Journal of Vibration Engineering & Technologies (2025) 13:105
https://doi.org/10.1007/s42417-024-01735-z

ORIGINAL PAPER

Theoretical and Experimental Investigation of the Use of a Roving Mass with Rotary Inertia for Crack Detection in Beam-Like Structures

X. Sun[1] · S. Ilanko[1] · Y. Mochida[1] · R. C. Tighe[1] · B. R. Mace[2]

Received: 16 May 2024 / Revised: 9 August 2024 / Accepted: 1 September 2024

Abstract

Purpose Natural frequency is a global dynamic parameter that normally contains limited spatial information on a crack in a structure. However, recently a theoretical concept that a roving mass with rotary inertia causes sudden frequency shifts when located near the crack location has been proposed as a method of locating cracks, although experimental verification is still lacking. This study fills this gap in knowledge, by investigating the measurability of the frequency shift as a roving body passes a crack.

Methods Natural frequencies were measured through impact hammer tests and compared with frequencies calculated using the dynamic stiffness method and finite element method.

Results The results show that the natural frequency shift could be clearly measured for a beam featuring a medium sized crack. For smaller cracks, while numerical results show that the current method would still enable the identification of their locations as frequency shifts are in the measurable range, the number of locations at which the measurement needs to be taken can be very large.

Conclusions This study provides insights into the practical feasibility of the roving mass technique for crack detection.

Keywords Roving mass · Rotary inertia · Crack detection · Beam · Impact hammer test · Dynamic stiffness method

Introduction

Vibration-based damage identification is a promising method in Structural Health Monitoring (SHM) to spot the existence of damage and assess the state of the entire structure [1]. In vibration-based methods, damage identification can be achieved by examining the changes in measured vibration response, such as modal parameters (natural frequencies, mode shapes, and modal damping), which are functions of the physical properties (mass, damping, and stiffness) of a structure [2]. Therefore, the changes in structural properties will result in variations in modal properties, which can either be detected absolutely or with reference to an undamaged state. By analysing these changes in modal properties, system identification can be performed to diagnose the structural health condition. This process involves solving inverse problems as it aims to extract the optimal mathematical model parameters so that the most feasible fit is obtained between the model output and the observed data [3].

Among the vibration-based methods, natural frequency-based methods have been researched extensively as frequency measurements can be quickly conducted and are cost-effective and often reliable. Compared with some non-destructive testing methods (such as microscopy, ultrasonic testing, thermography, etc.) that may require a labour-intensive and protracted process to inspect the whole structure, natural frequency-based methods offer an economical and effective approach for damage identification by using the natural frequency data collected from a single point on the structure. However, these methods have some disadvantages. For instance, significant cracks can lead to minor variations in natural frequencies, which may go undetected due to measurement errors [4]. In addition, the natural frequencies of the intact structure (i.e. baseline information) are not always available, thus many frequency-based methods endeavour to extract the spatial information of damage from the natural frequencies of the damaged structure alone.

✉ Y. Mochida
yusuke@waikato.ac.nz

[1] The School of Engineering, University of Waikato, Hamilton 3216, New Zealand

[2] Department of Mechanical and Mechatronics Engineering, University of Auckland, Auckland 1010, New Zealand

Published online: 16 January 2025

Consequently, the damage identification transforms into some challenging inverse problems where the damage location and severity are deduced from the natural frequency data of the damaged structure. For example, some natural frequency-based methods rely on an optimal criterion where the stiffness distribution of a structural element is iteratively adjusted to align the calculated natural frequencies with the measured frequencies at a specific level of damage [5]. These methods usually involve machine learning techniques [6] and optimisation algorithms [7, 8] in recent years.

To tackle the above issues, some researchers proposed methods incorporating an auxiliary mass to draw spatial information from the natural frequency shift caused by the mass passing the damage. As a result, baseline information is not required and the complexity of inverse problems can be largely avoided. Al-Said [9] proposed a method where a saw-cut crack was identified in a stepped cantilever beam carrying a slowly moving concentrated mass (i.e. a stationary roving mass) when the mass location coincides with the crack location. However, baseline information was still needed because the variation of the difference between the natural frequencies of cracked and intact systems versus each mass location was taken as the crack location index. Subsequently, Zhong and Oyadiji [10] applied a stationary wavelet transform to the curve of frequency versus mass location. The local perturbation caused by a crack was revealed and the crack was located. Yang and Oyadiji [11] found that the roving mass accentuated the local mode shape perturbations. By applying a discrete wavelet transform to the frequency-versus-mass-location curve, they observed that the approximation coefficients represented smooth components derived from the linear combination of the intact beam's mode shapes. In contrast, the local mode shape perturbations contributed to the detail coefficients. Consequently, these detail coefficients, characterized by high-order oscillations due to damage, could be isolated and utilized for damage detection. Zhang et al. [12] proposed the frequency shift surface methodology, which entails positioning an auxiliary mass at various points on a plate and observing changes in the fundamental natural frequency. In their study, they experimented with a steel plate featuring a central thickness reduction, supported by sponges to simulate free boundary conditions. A 0.3 kg accelerometer served as the auxiliary mass. Damage detection was achieved by analysing the fundamental frequency shift surface. This approach was subsequently extended to a damaged steel cylindrical shell [13]. By repositioning the auxiliary mass around the cylindrical shell's circumference, a frequency shift curve was produced, with the lowest point on the curve indicating the location of the damage.

Using an auxiliary mass as a probe for crack detection, Zhong et al. [14] proposed a method where an artificial quasi-interferogram fringe pattern (QIFP) and a high-speed camera were employed to improve the accuracy of natural frequency measurement. The QIFP was pasted on the surface of a vibrating cantilever beam as a sensor, and the image sequences of the QIFP were capture by a high-speed camera. Compared with using an accelerometer, the natural frequency shift when the mass passes the crack is more evident. Wang et al. [15] introduced the concept of a frequency shift path when a roving mass is attached to a beam. The frequency shift path is a spatial curve whose projection onto the time–frequency plane forms the frequency shift curve, while its projection onto the time–amplitude plane approximates the power of mode shape. Damages corresponding to 25% and 50% of beam thickness loss were introduced in the experiment and the curvature of frequency shift path was used as the crack location indicator. Apart from stationary roving mass, non-stationary mass (i.e. moving mass with velocity) has also been studied for crack detection, although not necessarily in combination with frequency measurement. For example, Lee and Eun [16] investigated the feasibility of damage detection using a moving mass and the effect of mass magnitude, mass velocity, and different measurement sensors were explored. Recently, Dadoulis and Manolis [17] analysed the dynamic response of a damaged beam model traversed by a heavy point mass for the purpose of damage detection. In their numerical studies, anomalies at the crack location were identified in the spectograms for the power spectral density function of the velocities as the point mass traverses the beam span from left to right. However, this finding still needs experimental validation, reducing the noise in data acquisition for effective crack detection can be challenging.

The roving mass technique has been utilized in crack detection for more complex structures. Lie et al. [18] expanded on the frequency shift curve method discussed in [13] to identify a sharp slot in a compressed natural gas cylinder by measuring the frequency shifts caused by an auxiliary mass. Cao et al. [19] simplified a parked vehicle-bridge interaction into a model where a beam supports a mass block. Wang et al. [20] employed an auxiliary mass to a railway track model to identify defects in the track supports, such as loose or missing fasteners and compromised ballast. This method proved particularly effective for detecting missing fasteners and severely damaged ballast. In certain cases when the damage cannot be inspected visually or when the damaged structure is inaccessible, the roving mass technique can be promising for damage detection. For example, the roving mass technique has been studied in detecting leakage and blockage faults in pipelines filled with fluid under acoustic excitation and without having to interfere with the operating of the pipelines [21–23]. It also seems promising in detecting internal defects such as interfacial debonding [11] in layered beams. Nguyen [24] investigated frequency-based crack detection in a double-beam system consisting

of two different beams connected by an elastic medium. The double-beam carried a roving mass and irregular changes in natural frequency were found when the mass was attached at the crack location. The study holds potential in crack detection for applications (e.g. multiple-walled carbon nanotubes, tall buildings, and continuous dynamic vibration absorbers) where the structure comprises elastically connected double beams. Haji and Oyadiji [25] employed a roving disc traversing along the length of a non-rotating rotor to amplify crack effects. The natural frequencies of the cracked rotor in two lateral bending vibration planes were used to develop the crack location index and the crack was identified through sharp, notched peaks in the curve of the normalised orthogonal natural frequency.

In previous studies involving a roving mass, only the translational inertia was considered, with the effect of rotary inertia being neglected. Cannizzaro et al. [26] showed that when a roving body with both mass and rotary inertia moved past a crack, the natural frequencies of a beam exhibited abrupt changes. Following this, Ilanko et al. [27] conducted a numerical analysis of frequency variations as a roving body traversed a crack on a plate. They observed a sudden frequency shift when the roving body with rotary inertia crossed a partial crack, and a similar shift with translational inertia only when crossing a complete crack. These abrupt natural frequency shifts identified in [26, 27] could be used to locate cracks. While these studies provided numerical evidence, experimental validation is still lacking to confirm the presence and detectability of the natural frequency shift. Furthermore, the assumption that rotary inertia acts at a point in theoretical derivations may not hold true in practice, causing what should be an abrupt frequency jump to possibly appear as a steep change, thereby complicating the detection of the frequency shift.

This study endeavours to fill the above gap in knowledge. Compared with previous studies utilizing the roving mass technique for natural frequency-based crack detection, this study for the first time considers both mass and rotary inertia in the experiment design, and the measurability of the frequency shift caused by the roving mass with rotary inertia passing a crack with regard to the crack severity is investigated. Additionally, this study presents a direct comparison between experimental, theoretical, and simulation results, providing insights into the practicality of measuring theoretically significant natural frequency changes using impact hammer tests. To be specific, impact hammer tests were conducted on two cracked beams carrying a roving mass with rotary inertia. The experimental frequency results are compared with the results obtained using the dynamic stiffness method (DSM) and the finite element method (FEM). To obtain accurate results through the DSM, Rayleigh bar theory and Timoshenko beam theory are combined when constructing the dynamic stiffness matrix of an individual element, and the Wittrick–Williams algorithm is employed to extract natural frequencies. Based on the experimental results, the feasibility of using the natural frequency shift caused by a roving mass with rotary inertia passing a crack for crack detection is discussed. It is worth noting that the mass roves on the beam, and whenever the mass is located in a new position, the natural frequencies of the beam are evaluated. Therefore, the mass is considered stationary in this study.

Experiments

This section elaborates on the experimental work conducted to investigate the existence and measurability of the natural frequency shift, including the design, instrumentation, and preparation before experiments.

Experiment Layout

The overall layout of the experimental set-up is shown in Fig. 1. A heavy steel platform with two supports was designed to carry a beam. The beam was clamped to the support at each boundary using a cap and two M8 × 30 mm bolts. The beams used in this experiment were made of mild steel with a density of 7571.4 kg/m^3. The beam was 2 mm thick and 20 mm wide. The length of the beam L between the boundaries was 623 mm.

A crack was simulated by machining a cut-out on the beam. Two crack depths were used, corresponding to 20% and 40% thickness reduction of the beam, respectively. As an example, Fig. 2 shows the appearance of a 20% crack. The opening of the slot was 2 mm wide. The distance between the left boundary and the left edge of the crack was 393 mm.

The roving mass was made of steel and weighed 1.15 times the weight of the beam. Although the roving mass does not have to be heavy, to achieve a measurable change in natural frequencies (i.e. Δf) in the first few natural frequencies when the mass passes the crack, a heavy mass would be favourable. Some trial calculations were conducted when determining the weight of the mass to make sure that the maximum stress in the beam was far from yield after attaching the mass to the beam. As shown in Fig. 3, the radius of gyration of the roving mass was designed to be adjustable, hence the rotary inertia of the mass can be adjusted.

A detailed view of the connection between the roving mass and the beam is given in Fig. 4. The roving mass was clamped to the beam using M4 bolts and nuts. Whenever the mass was located in a new position, the M4 bolts were tightened. After finishing each impact hammer test, the bolts were loosened thus the mass could be moved to the next position. To minimize the roving step size, the contact area between the roving mass and the beam was set to a width of

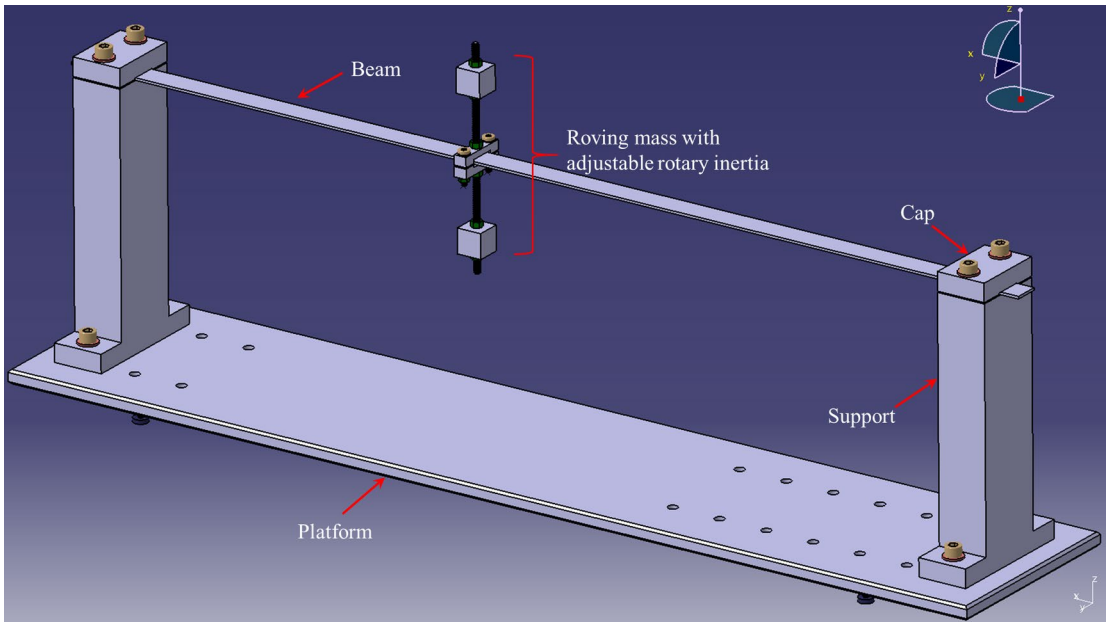

Fig. 1 The overall layout of the experimental set-up

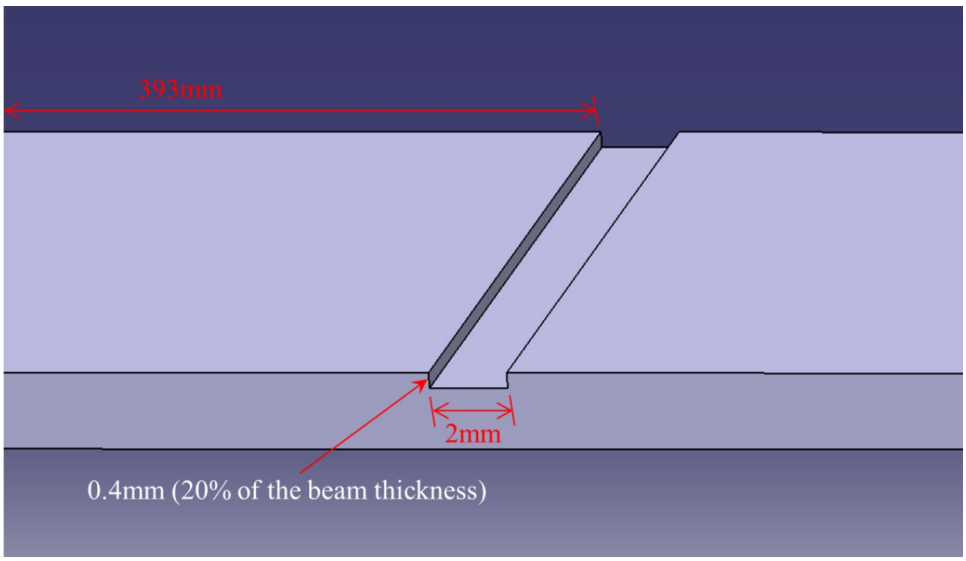

Fig. 2 The segment of a 20% cracked beam

2 mm (see Fig. 4b). Figure 5 shows the mass locations near the crack. Each shadowed area represents the contact area between the mass and beam at each mass location. It can be seen that 4 mm is the minimum roving step size that can be achieved using this set-up.

Impact Hammer Tests

Impact hammer tests were performed to measure the frequency response of the set-up at an ambient temperature of about 21 °C. The set-up for the impact hammer tests is shown in Fig. 6. The impact hammer (PCB model: 086E80) had a soft tip with the impact location at a distance of 82 mm from the right boundary of the beam, and the beam response was measured by an accelerometer (PCB model: TLD352A56) attached underneath the beam at a distance of 244 mm from the left boundary of the beam. The roving range on the beam was limited to 280 mm (see Fig. 6) to allow space for the impact point, the accelerometer, and the cable. The excitation and response signals were then processed by a dynamic signal analyser (model: Data Physics QUATTRO) which gave the transfer function.

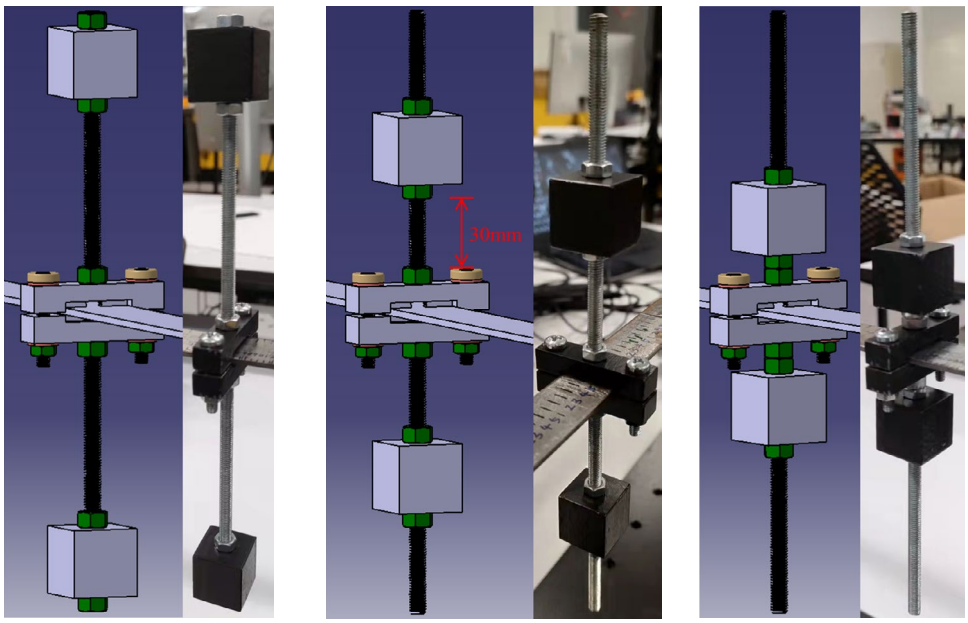

(a) maximum setting (b) medium setting (c) minimum setting

Fig. 3 Different settings of the rotary inertia (design figures and real photos)

It was necessary to configure some parameters for the signal analyser, for example, the bandwidth f_H, sampling frequency f_s, triggering, windowing, and the number of averages. Preliminary numerical studies showed that a bandwidth of 800 Hz was sufficient to measure the first eight natural frequencies. The sampling frequency was set to be 2048 thus $f_s > 2f_H$ which satisfied the Nyquist criterion [28]. The resulting frequency resolution Δf was 0.03125 Hz, the time span T was 32 s, and the time resolution ΔT was 1/2048s. The trigger was set to start data acquisition when the impulse from the hammer reached 0.5 N. A delay of -5% was selected, i.e. the acquisition began 0.05 ΔT earlier than the triggering event. A rectangular window was used. Five measurements for each mass location were recorded and averaged. Double impact or overloaded tests were rejected. The time histories were stored and processed to obtain the transfer function and coherence. The setting of the above parameters and the data analysis and visualisation were conducted using SignalCalc 900 Series software (see Fig. 7). The data file containing the transfer function signal was then exported for post-processing in MATLAB using the single-degree-of-freedom (SDOF) circle-fit method [29, 30].

Preparation Before the Measurement

Tensile Test

The Young's modulus of the mild steel used for manufacturing the beams was determined through a tensile test using an Instron universal testing machine with a 5 kN load cell, following the tensile testing standard for metallic materials (ISO 6892-1:2009(E)). Six parallel-sided strip samples were prepared. The maximum force was set to 4.5 kN. A mechanical extensometer with a nominal gauge length of 50 mm was attached to the sample to measure the elongation. A crosshead separation rate of 1.05 mm/min was applied. The modulus calculation was performed by the Instron Bluehill material testing software using the data in the strain range of 0.025%–0.035%. For each sample, five tests were repeated and the results were averaged. Then the results of the six samples were averaged. In the end, the average Young's modulus of the samples was found to be 188.6 GPa.

Repeatability and Reciprocity Checks

Repeatability checks are generally required to assess the stability of structural characteristics over a period of time. In this experiment, the bolts of the roving mass were tightened by hand to approach a rigid connection between the mass and beam. After an impact hammer test, the bolts were loosened to reposition the mass. Once the mass was in position, the bolts were tightened again followed by another hammer test. In this process, the torque of the bolts might slight changes in the natural frequencies. Therefore, it was important to check the repeatability of natural frequency results by loosening the bolts and retightening them. With an acceptable repeatability check, the variance caused by the torque of bolts could be ignored, and the change of natural frequencies could be assumed only due to the crack and roving mass.

Figure 8 shows the transfer functions of five repeatability tests conducted on an intact beam carrying the roving mass with the maximum rotary inertia setting. The distance between the mass location and the left boundary of the

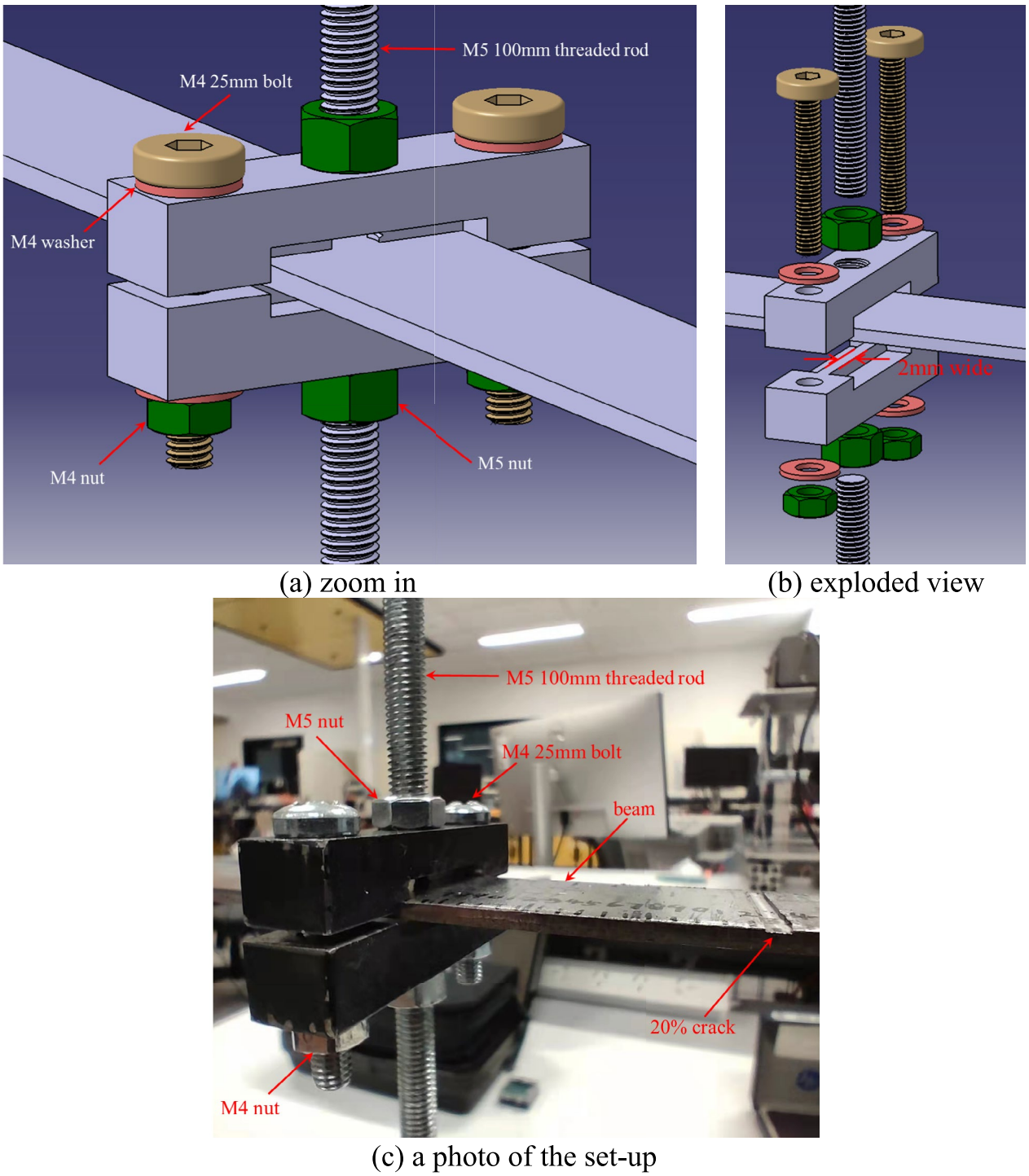

Fig. 4 The detailed view of the connection between the roving mass and beam

beam was 0.36 m. In between successive tests, the mass was removed from the beam and then reinstalled. It can be noted that the five curves of the transfer function are almost identical, demonstrating excellent repeatability of the test. Table 1 displays the first eight natural frequencies of the repeatability tests and the standard deviation between the tests. The results exhibit minor variance, which also proves the excellent repeatability.

Apart from the repeatability check, the reciprocity of tests was checked by confirming that the measured transfer function for an impact at location i and a response at location j agrees well with the transfer function measured

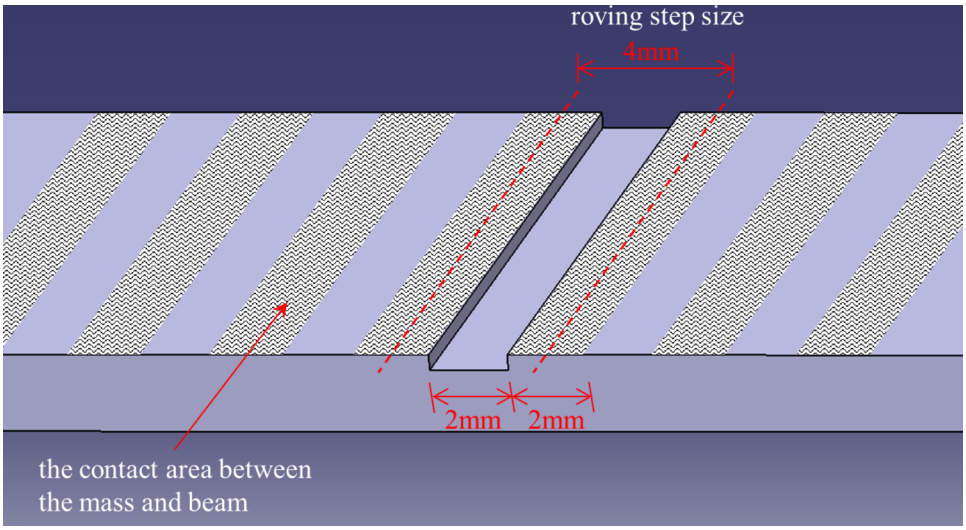

Fig. 5 The mass locations near the crack

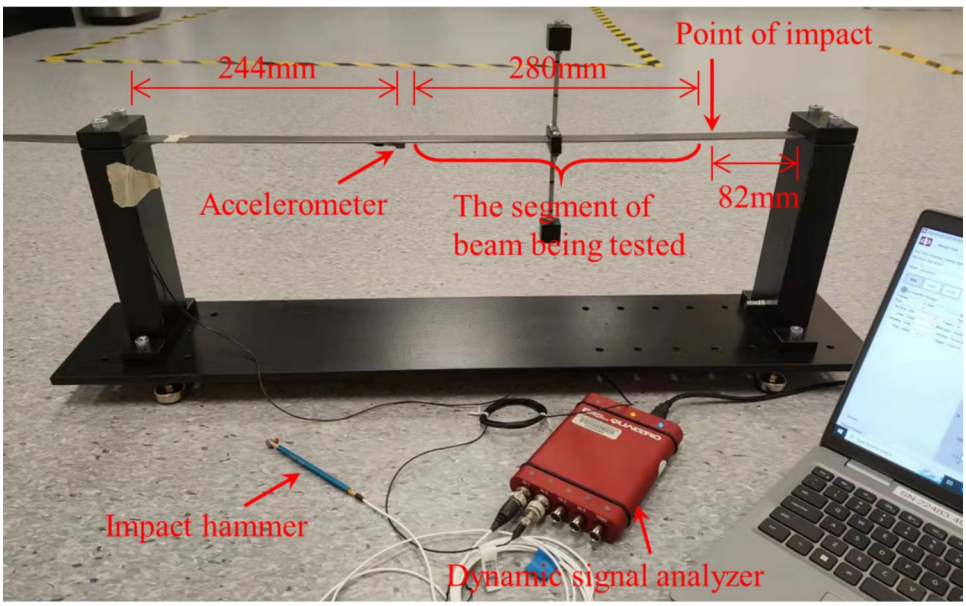

Fig. 6 The set-up for impact hammer tests

for the same impact (approximately) at location j and a response at location i. The results were found similar to those in Fig. 8 and are not reported here.

Simulation of the Experiment

An FE model was created using ANSYS Mechanical APDL to simulate the vibration of the experimental set-up. Considering the irregular shape of the set-up, SOLID187 elements (higher order 3D 10-node elements with a quadratic displacement behaviour) were used to discretize the model. Free meshing was used to mesh the model. The APDL was compiled in such a way that the roving mass and the cracked beam were generated as a whole body (to simulate the rigid connection between the mass and beam), and the process of creating the model was packaged in a macro. Modal analysis was performed whenever the mass location was changed. Some trial calculations were conducted by modifying the level of element size until the natural frequency results converged. Figure 9 shows a typical discretization of the model when the rotary inertia is at the maximum setting.

Analytical Model of the Experiment

Apart from the FE model, a simplified analytical model of the experimental set-up was created using the DSM. The DSM involves finding the dynamic stiffness of individual

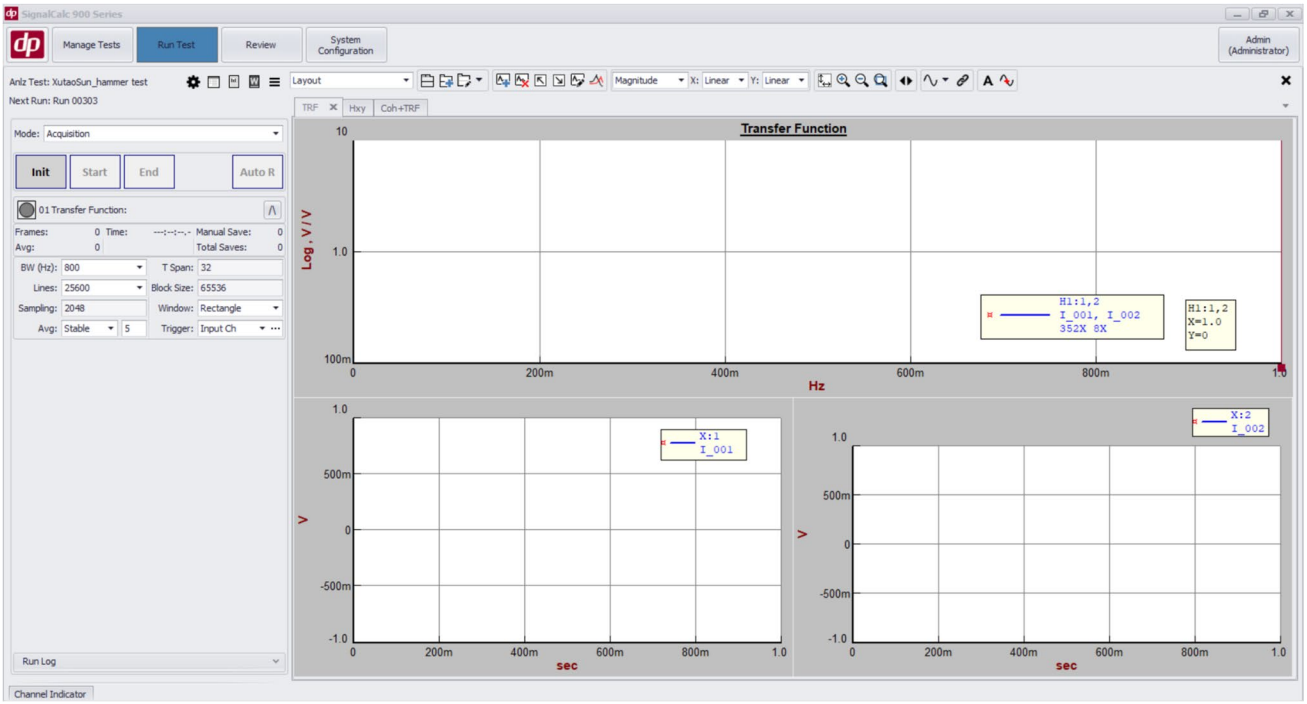

Fig. 7 The user interface of SignalCalc 900 Series software

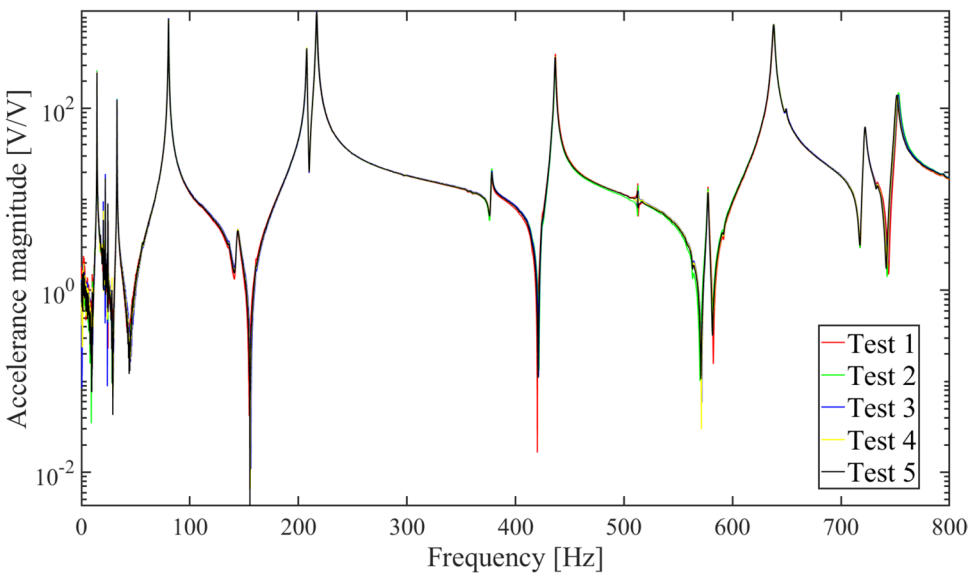

Fig. 8 The transfer functions of five repeatability tests

components of the structure by analytically solving the governing equations and assembling these to form the dynamic stiffness matrix for the structure. For free vibration, the determinant of this matrix is zero, which leads to a transcendental equation whose roots give the natural frequencies. In the past, the DSM has been applied to structural members such as beams [31, 32], plates [33, 34], and shells [35, 36]. The DSM was also used in problems involving cracked members to investigate the dynamic response of structures in the presence of a crack [37–41]. To solve the transcendental dynamic stiffness matrix equation, a reliable eigensolver is required and the Wittrick–Williams algorithm is well suited for this. The Wittrick–Williams algorithm [42, 43] is an efficient eigensolver that appears frequently within the DSM literature. It searches for eigenvalues in such a way that there is no possibility of missing any one of them.

The dynamic stiffness matrix of a beam element is given in [31, 44]. For a crack element, its dynamic stiffness matrix

Table 1 The natural frequency results of five repeatability tests

Mode number	Natural frequency results (Hz)					Standard deviation
	Test 1	Test 2	Test 3	Test 4	Test 5	
1	14.40	14.40	14.39	14.39	14.39	0.003
2	32.86	32.88	32.88	32.86	32.83	0.021
3	80.48	80.42	80.37	80.33	80.29	0.075
4	144.5	144.1	144.0	143.5	143.5	0.420
5	217.1	217.0	216.9	216.9	216.9	0.088
6	378.0	378.2	378.1	378.1	377.9	0.130
7	436.8	436.8	436.7	436.6	436.6	0.094
8	638.1	638.0	638.1	638.1	637.9	0.074

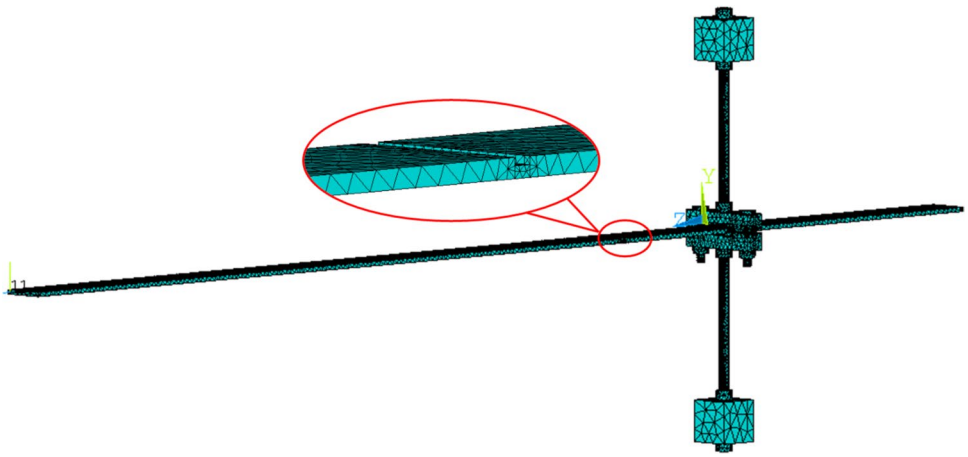

Fig. 9 A typical discretization of the model in ANSYS

can be obtained from the 3×3 flexibility matrix as given in [45]. The global dynamic stiffness matrix can be constructed following a proper assembling process. For this study, the effect of concentrated translational and rotary inertia was considered by modifying the associated diagonal terms of the global dynamic stiffness matrix. The Wittrick–Williams algorithm was employed to calculate natural frequencies. For the completeness of this study, the relevant information is provided in the supplementary data.

Mode shapes obtained using ANSYS and DSM are shown in Fig. 10. A beam with a 40% crack was modelled and the mass with the maximum rotary inertia setting was located 76 mm on the right side of the crack. For the DSM mode shapes, the red triangle and green dot indicate the crack location and mass location, respectively.

From Fig. 10, the mode shape results obtained using the two methods are in good agreement. Although the DSM model was a simplified 2D model, it still predicts the mode shapes of the beam accurately. The ANSYS model was a 3D model and included more details of the roving body. Apart from the bending modes shown in Fig. 10, some torsional modes and bending modes in the strong direction of the beam (which may also appear in the experiment) were also obtained from the ANSYS model. Figure 11 shows two examples of these modes. Overall, the results from the ANSYS model were closer to the experiment results, and this will be discussed in the next section through natural frequency comparison.

Results and Discussion

Figure 12 shows the schematic diagram of the experimental set-up for impact hammer tests. A total of 71 mass locations were tested on each cracked beam. The coordinate of the centre of the crack is 394 mm. The coordinates of mass locations on the immediate left side and right side of the crack were 392 mm (the 35th mass location) and 396 mm (the 36th mass location), respectively.

For each cracked beam, three settings of rotary inertia as shown in Fig. 3 were tested. As an example, the natural frequency results of a cracked beam carrying a roving mass with the maximum rotary inertia setting are presented in the following sections.

40% Cracked Beam

The comparison of natural frequency results obtained through experimental measurement, ANSYS, and DSM is shown in Fig. 13. The results are in good agreement,

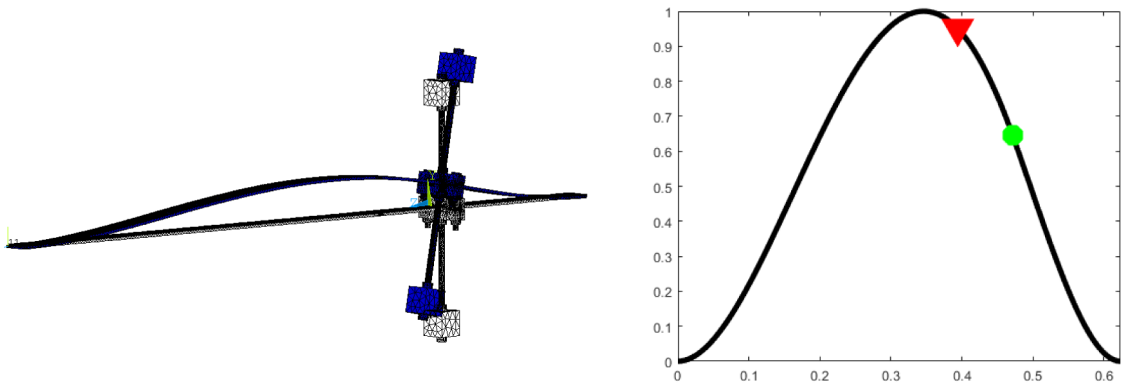

(a) 1st mode shape

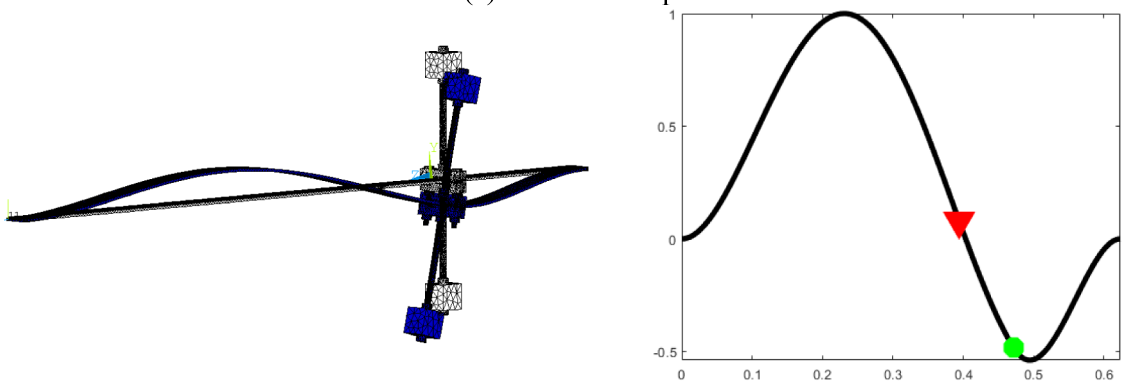

(b) 2nd mode shape

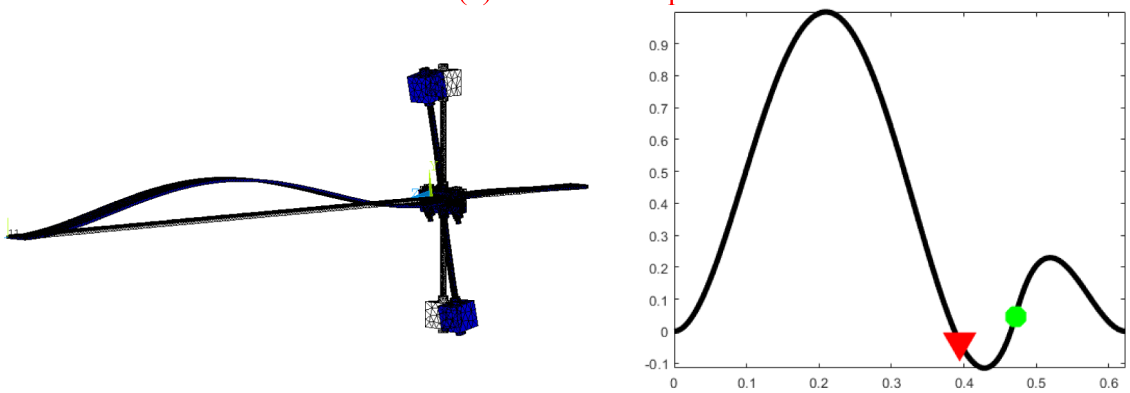

(c) 3rd mode shape

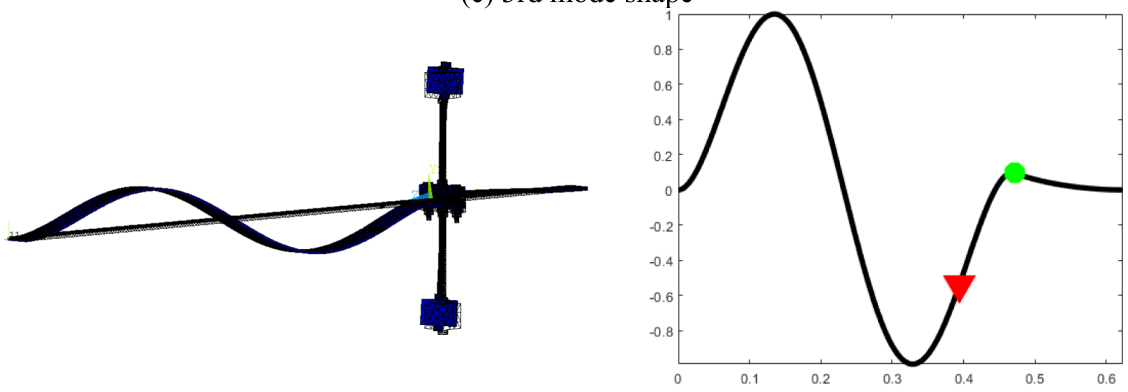

(d) 4th mode shape

Fig. 10 The comparison between ANSYS mode shapes (left side) and DSM mode shapes (right side, with the red triangle and green dot indicating the crack location and mass location, respectively)

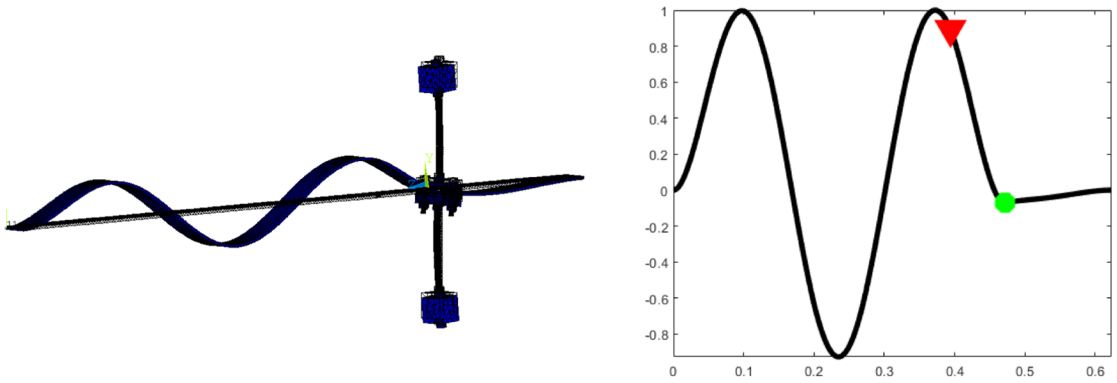

(e) 5th mode shape

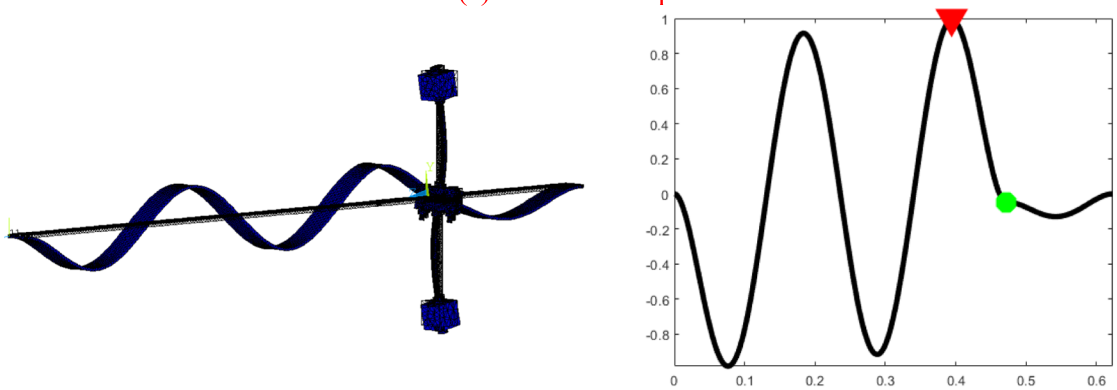

(f) 6th mode shape

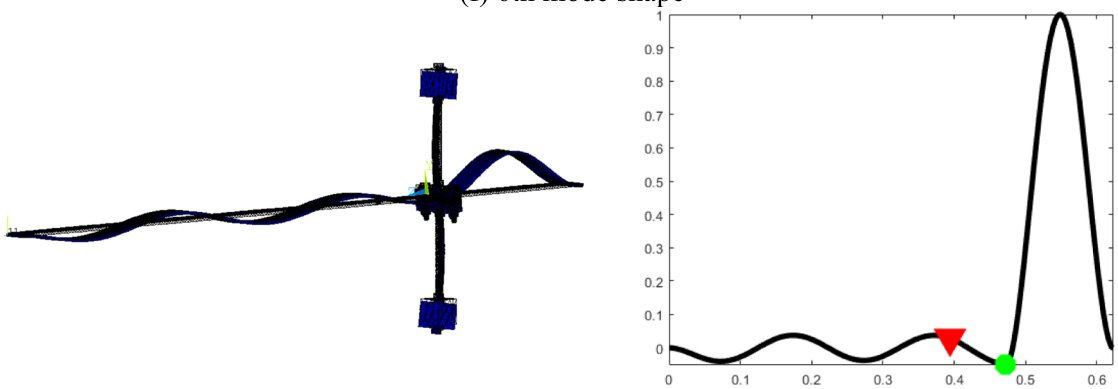

(g) 7th mode shape

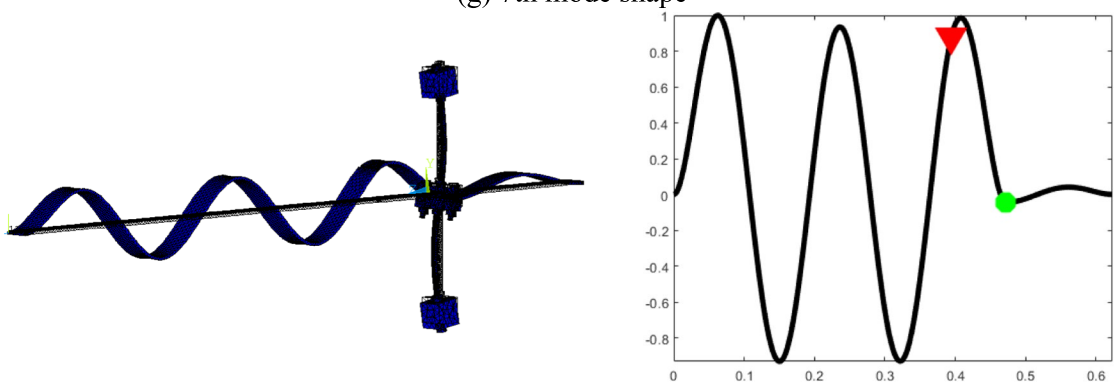

(h) 8th mode shape

Fig. 10 (continued)

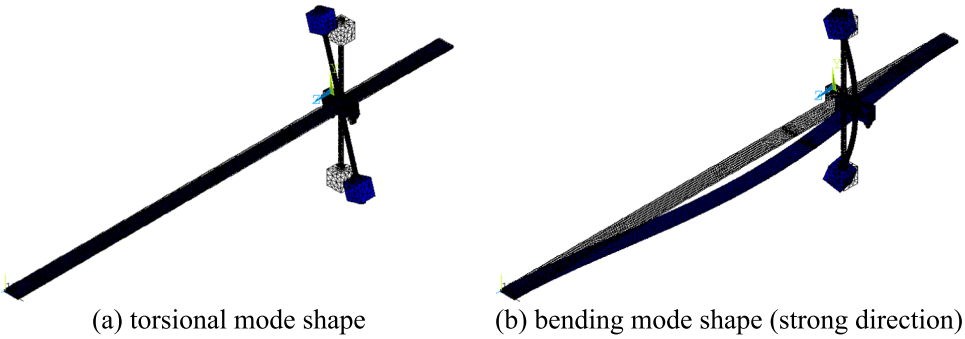

(a) torsional mode shape (b) bending mode shape (strong direction)

Fig. 11 Two examples of the out-of-plane modes in ANSYS results

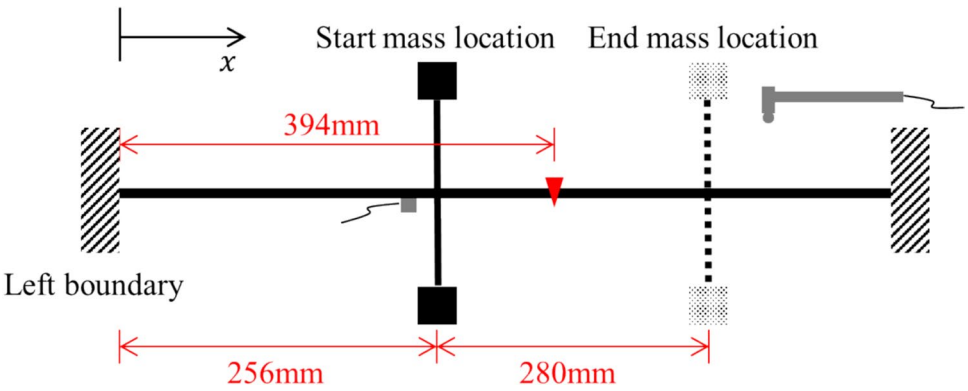

Fig. 12 The schematic diagram of the experimental set-up

demonstrating the satisfactory accuracy of the ANSYS model and DSM model. Among the three sets of results, DSM results generally give the highest frequencies, followed by ANSYS results. Experimental results are mostly the smallest. The main reason why DSM results are generally larger than ANSYS results is due to the simulation of the crack. As shown in the supplementary data, the crack was modelled through three zero-length mass-less springs in the DSM model, while in the ANSYS model, both the crack depth and crack opening were considered. Therefore, the stiffness of the DSM model should be higher than that of the ANSYS model, leading to higher natural frequencies. Similarly, the phenomenon that ANSYS results are normally larger than the experimental results may also be attributed to the difference in stiffness. For the ANSYS model, the boundary conditions were ideal and no relaxation between the mass and beam was allowed. Both conditions were difficult to achieve in the experiment where the clamped boundaries and rigid connection could only be approximated. All these factors would decrease the natural frequencies of the experimental set-up when compared with the simulation. However, the ANSYS model still gave good predictions of natural frequencies, with the average relative percentage error between experimental results and ANSYS results for the first eight natural frequencies ranging from 2.7 to 8.2%.

From Fig. 13, the natural frequency shift predicted by both the DSM model and ANSYS model when the mass passed the crack at 394 mm can be observed in the experimental results. Thus, in this case, the natural frequency shift caused by a roving mass with rotary inertia passing a crack is experimentally verified. It is worth noting that there are two abnormal frequency shifts in the fifth natural frequency (Fig. 13e) when the mass location is around 364 mm and 480 mm. This is because there was a closely neighbouring mode (as shown in Fig. 11b) near the fifth bending mode when the mass was near those two locations. In this situation, the SDOF assumption of the circle-fit method [46] was not satisfied and hence the extracted natural frequencies were not accurate. However, this phenomenon only happened for certain natural frequencies at some mass locations (approximately ten mass locations in the fifth natural frequency). Overall, the circle-fit method delivered good results.

To examine the measurability of the natural frequency shift, the difference between the natural frequencies obtained when the mass is located in two adjacent positions were calculated consecutively. For example, when the mass roves to a new position, the natural frequency of the previous position (denoted by f_{pp}) is subtracted from that of the current position (denoted by f_{cp}), leading to the natural frequency shift at the current position

$$\Delta f_{cp} = f_{cp} - f_{pp} \tag{1}$$

Repeating this procedure for the natural frequencies at all mass locations, the resulting curves of natural frequency

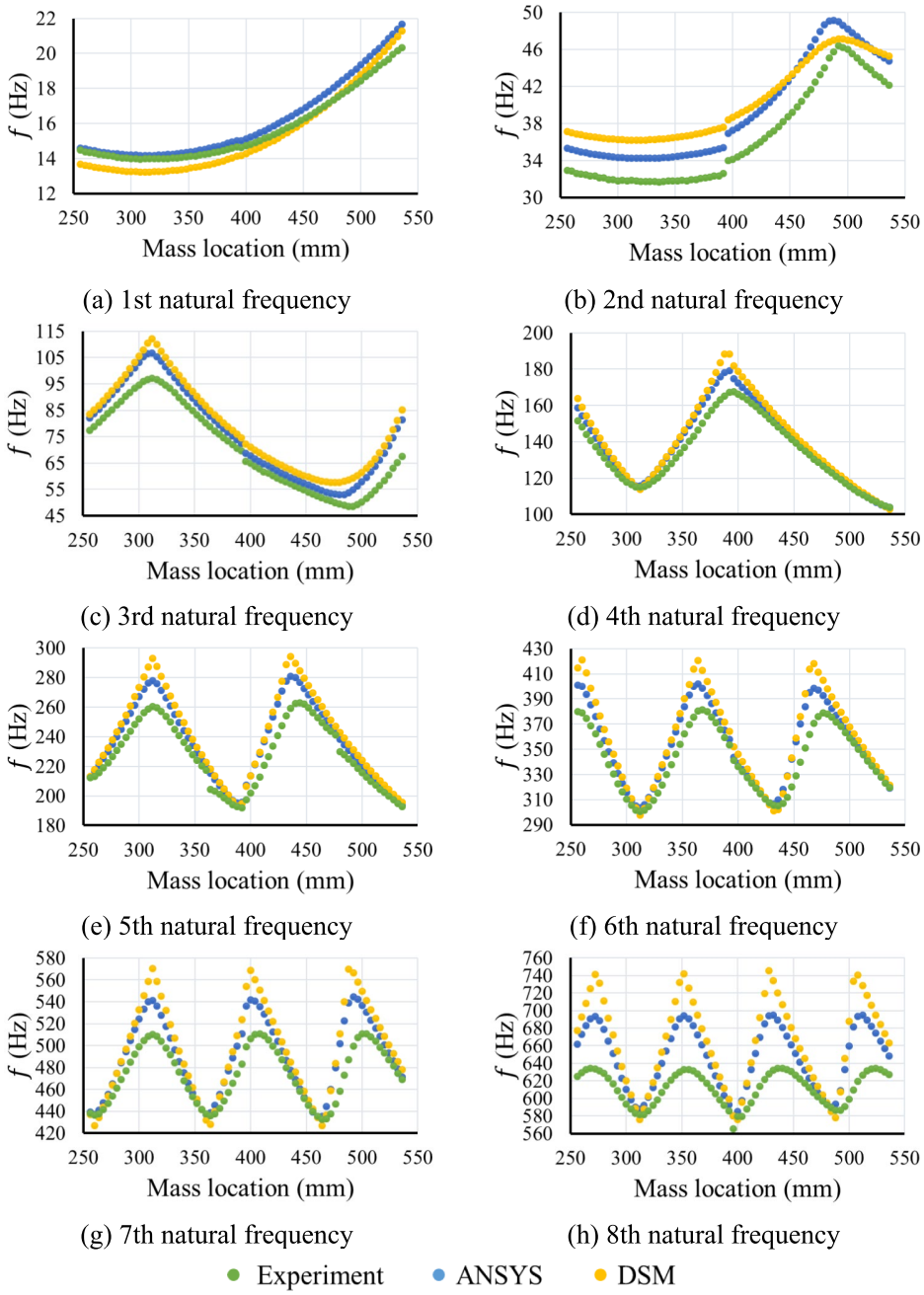

Fig. 13 Measured and predicted natural frequencies (40% crack located at 394 mm)

shift Δf are shown in Fig. 14. For the first three natural frequencies, the crack location is clearly indicated by the peak in the curve of Δf. For the fourth and fifth natural frequencies, the peak at the crack location is not obvious. Two false peaks are present in the curve of Δf for the fifth natural frequency (Fig. 14e) due to closely coupled modes as explained above. For the sixth to eighth natural frequencies, the peak at the crack location is still noticeable despite more fluctuations appearing in the curve of Δf.

In general, the natural frequency shift when the roving mass with rotary inertia passes the crack can be clearly measured for the 40% cracked beam. It is possible to pinpoint the crack location by observing the peak in the curve of Δf versus mass location. Next, it is necessary to check whether the frequency shift is still measurable for a 20% cracked beam.

20% Cracked Beam

For the 20% cracked beam, the comparison of natural frequency results is shown in Fig. 15. The results obtained through the different methods are still in good agreement.

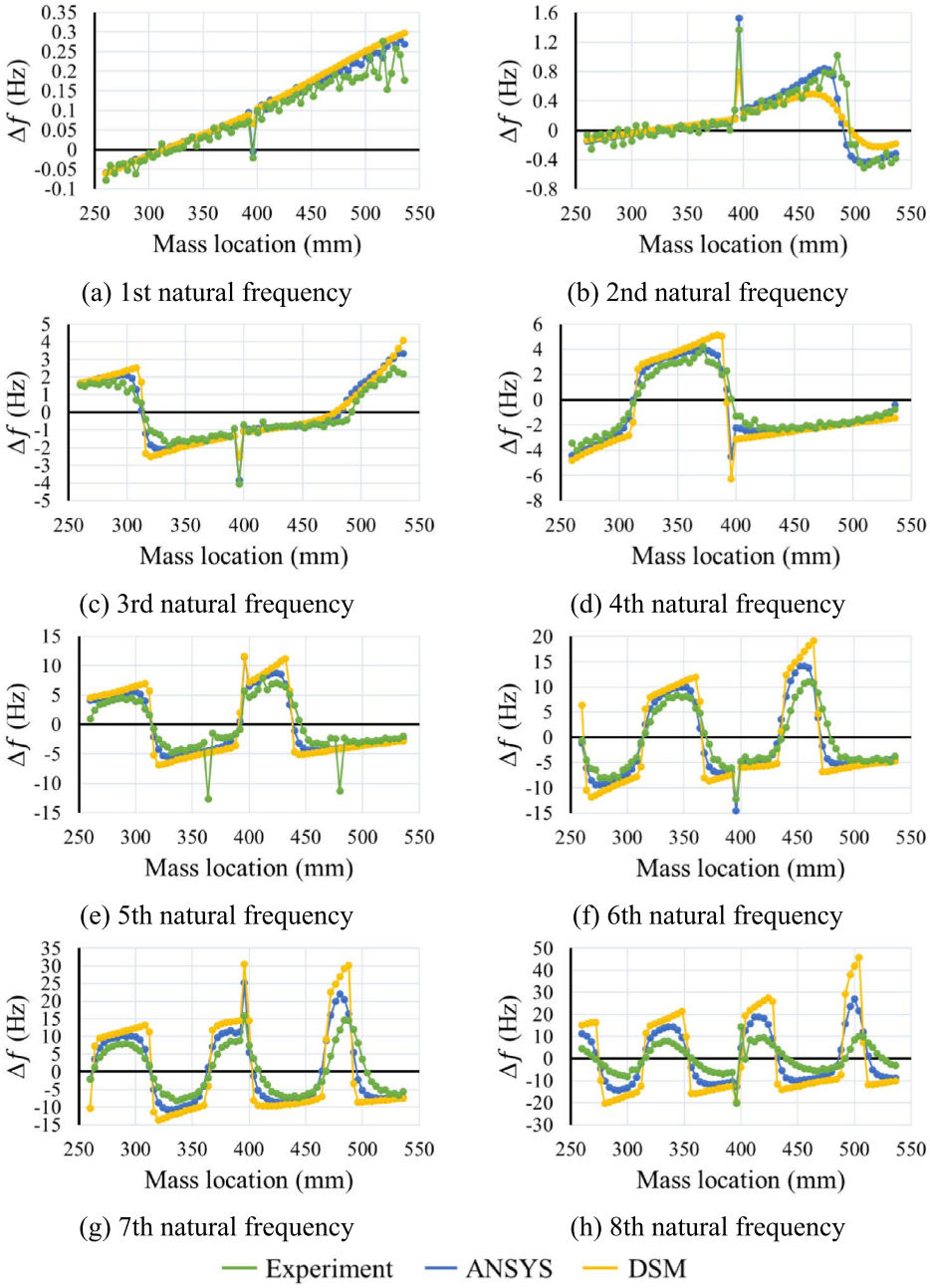

Fig. 14 Measured and predicted natural frequency shift (Δf) (40% crack located at 394 mm)

The average relative percentage error between experimental results and ANSYS results for the first eight natural frequencies is between 2.5 and 8.2%. However, the natural frequency shift that happens when the mass passes the crack at 394 mm is difficult to observe directly from the curve of natural frequency. Besides, some abnormal frequency shifts may affect the estimation. For example, in the curves of the fourth and fifth natural frequencies, some abnormal frequency shifts appear because these two modes are closely coupled with two out-of-plane modes when the mass is located at certain locations. In the curve of the second natural frequency, when the mass location is approaching 500 mm, an abnormal frequency shift exists possibly due to measurement error or beam internal defects. Therefore, it is necessary to check the measurability of the natural frequency shift Δf. The results are shown in Fig. 16.

From Fig. 16, the peak in the curve of Δf when the mass passes the crack location can be observed. However, the magnitude of the peak is much smaller compared with Fig. 14. For example, it is impossible to find a noticeable peak at the crack location for the first natural frequency. For the second natural frequency, the peak at the crack location

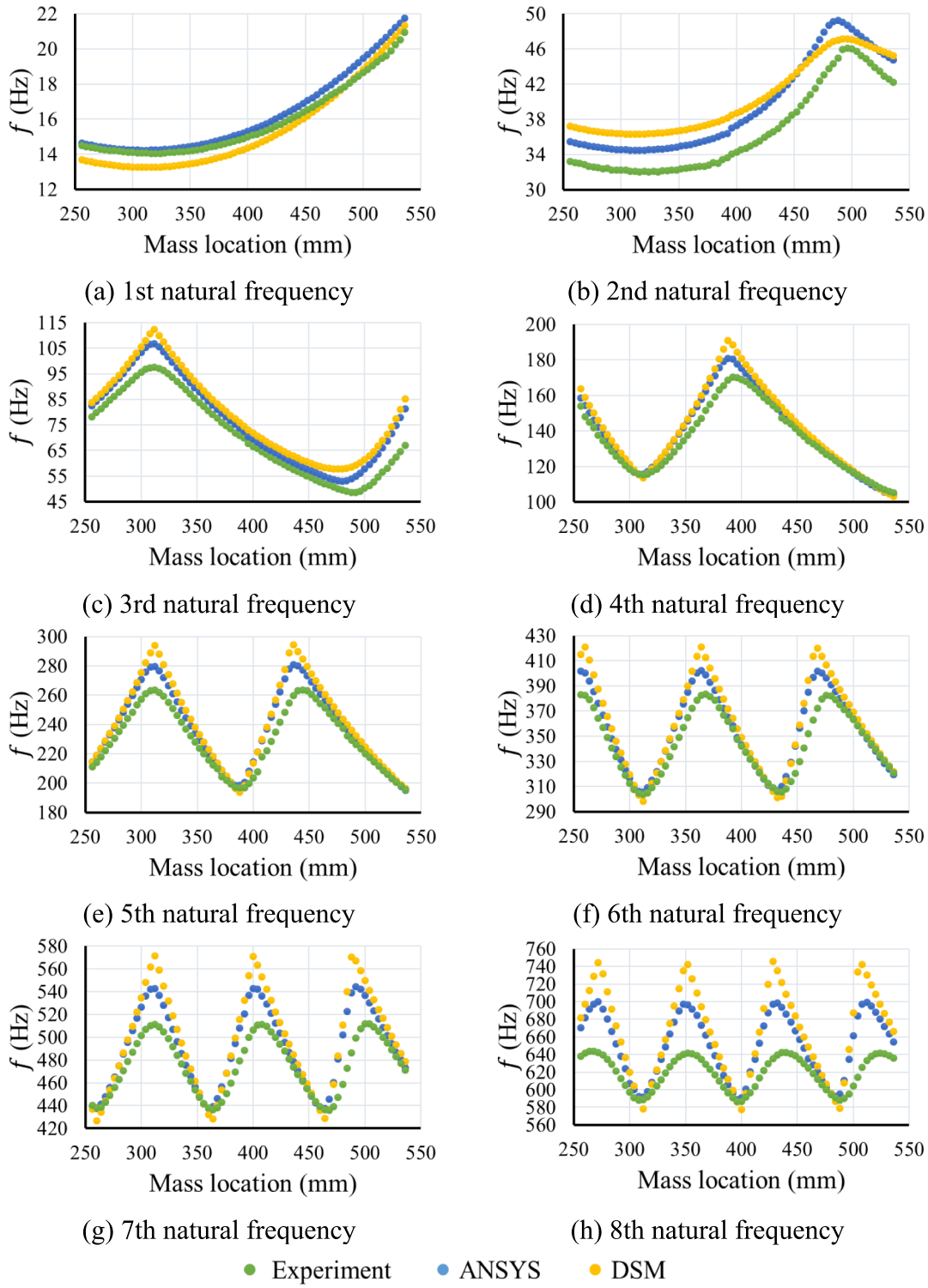

Fig. 15 Measured and predicted natural frequencies (20% crack located at 394 mm)

is observable. However, the magnitude of the peak is comparable to that of the peak caused by measurement error. False peaks appear in the curves of Δf of the fourth and fifth natural frequencies (Fig. 16d, e) due to closely coupled modes. For the sixth to eighth natural frequencies, the peak

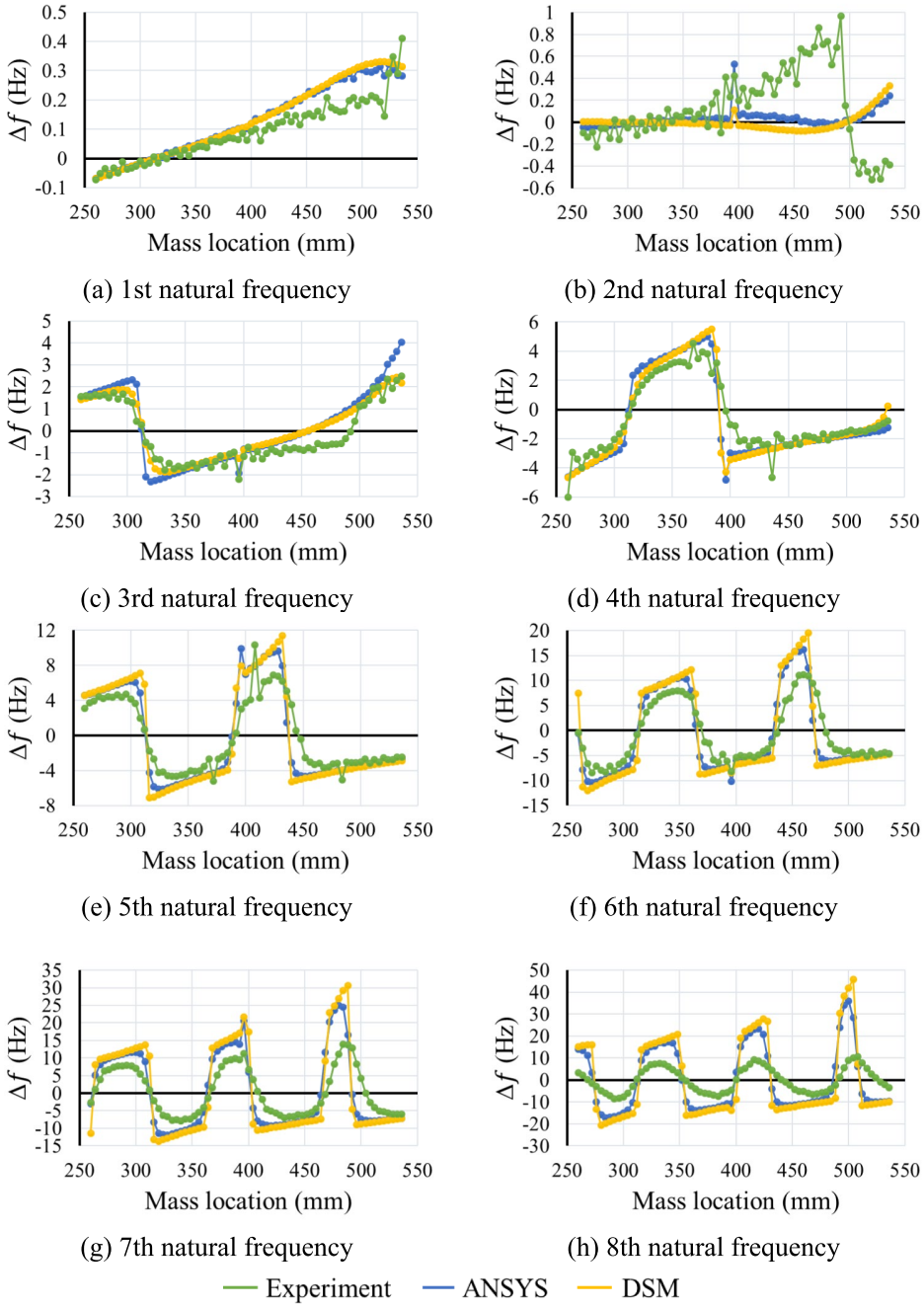

Fig. 16 Measured and predicted natural frequency shift (Δf) (20% crack located at 394 mm)

at the crack location is discernible but not obvious enough due to the fluctuation of the curves.

To highlight the crack location, the change of natural frequency shift (i.e. $\Delta(\Delta f)$) is calculated. $\Delta(\Delta f)$ is defined as follows. f_{pp}, f_{cp}, and f_{np} are used to denote the natural frequencies when the mass is located in the previous position, the current position, and the next position, respectively. The natural frequency shift of the current mass position, i.e. Δf_{cp}, is given in Eq. (1). Similarly, the natural frequency shift of the next mass position, i.e. Δf_{np}, is written as

$$\Delta f_{np} = f_{np} - f_{cp} \tag{2}$$

The change of natural frequency shift when the mass is located in the next position, i.e. $\Delta(\Delta f_{np})$, is expressed as

$$\Delta\left(\Delta f_{np}\right) = \Delta f_{np} - \Delta f_{cp} \tag{3}$$

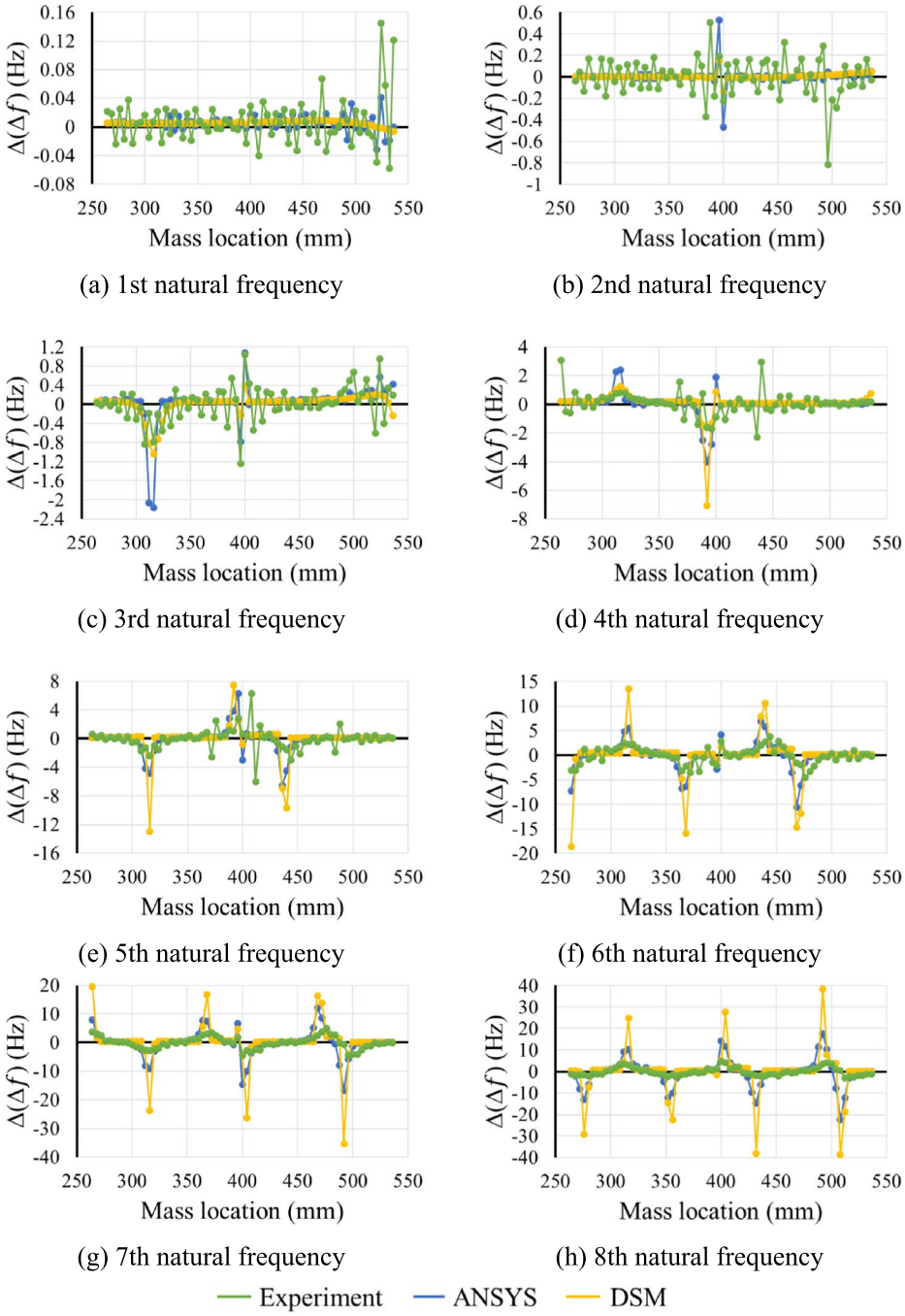

Fig. 17 Measured and predicted natural frequency shift (20% crack located at 394 mm)

Therefore, $\Delta(\Delta f)$ is the difference between the Δf when the mass is located in two adjacent positions.

The results of $\Delta(\Delta f)$ are shown in Fig. 17. Although there are some shifts in this parameter at the crack location for some modes, it is difficult to pinpoint the crack location due to the presence of some false peaks. These false peaks are generally due to measurement error or the small natural frequency shift around the extrema of the curve of natural frequency. As an example, Fig. 18 shows the comparison of f, Δf, and $\Delta(\Delta f)$ for the eighth natural frequency. The red dotted lines indicate the mass locations corresponding to the extrema of the curve of natural frequency. It can be seen that Δf changes in sign around these locations, leading to peaks in the curve of $\Delta(\Delta f)$. In magnitude, these peaks are comparable to the peak when the mass passes the crack location, making it difficult to determine the crack location from the curve of $\Delta(\Delta f)$.

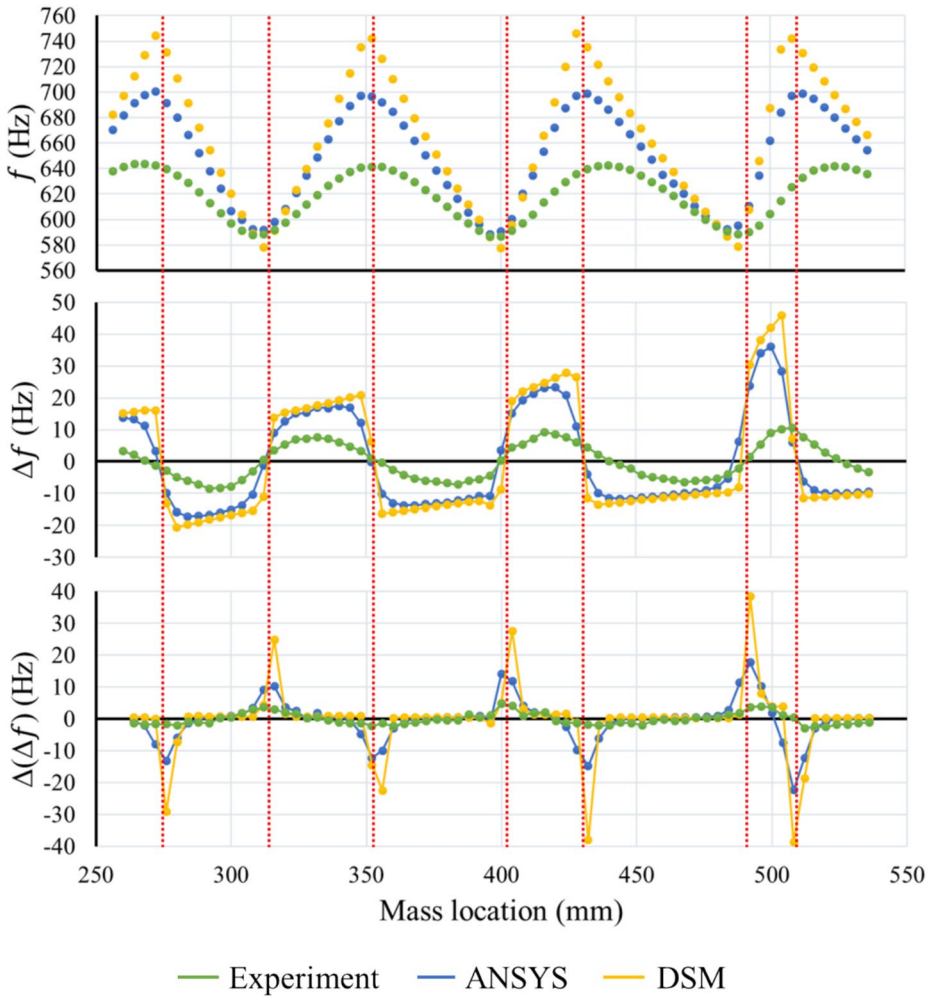

Fig. 18 The comparison of f, Δf, and $\Delta(\Delta f)$ for the eighth natural frequency

In general, the natural frequency shift when the roving mass with rotary inertia passes the crack can still be measured for the 20% cracked beam. However, it can be difficult to pinpoint the crack location by observing the peak in the curve of Δf or $\Delta(\Delta f)$ versus mass location. For the curve of Δf, the magnitude of the peak at the crack location is small for lower frequencies. For higher frequencies, the magnitude increases, but the fluctuation of the curve also becomes greater, which makes the peak at the crack location less discernible. For the curve of $\Delta(\Delta f)$, the curve is flatter and the peak is more obvious. However, the presence of some false peaks hampers the determination of crack location.

Further Numerical Studies

From the above experimental results, the curves of Δf and $\Delta(\Delta f)$ versus mass location for higher modes can help locate the crack. However, fluctuations in the curve of Δf and ensuing false peaks in the curve of $\Delta(\Delta f)$ are also common in higher modes. If decreasing the ratio of step size to structure length, it is possible to reduce the magnitude of Δf between two adjacent mass locations, hence making the frequency change when the mass passing the crack more prominent. Although this would inevitably demand more sampling locations and longer measurement time, it is instructive to examine the results through a numerical study.

In the following study, the step size is maintained at 4 mm but the length of the beam is scaled up. The length, width, and thickness of the beam are increased by factors of 10, 40, and 80, respectively. Now the beam is 0.16 m thick and 0.8 m wide, and the length of the beam L is 6.23 m. The magnitudes of the translational and rotary inertia of the roving mass are also increased in proportion, thus the ratio between the roving mass and beam is the same as the maximum value used in the experiment. A 10% crack is studied with the crack opening remaining 2 mm wide and the crack depth being 16 mm. The location of the crack is now 3.94 m.

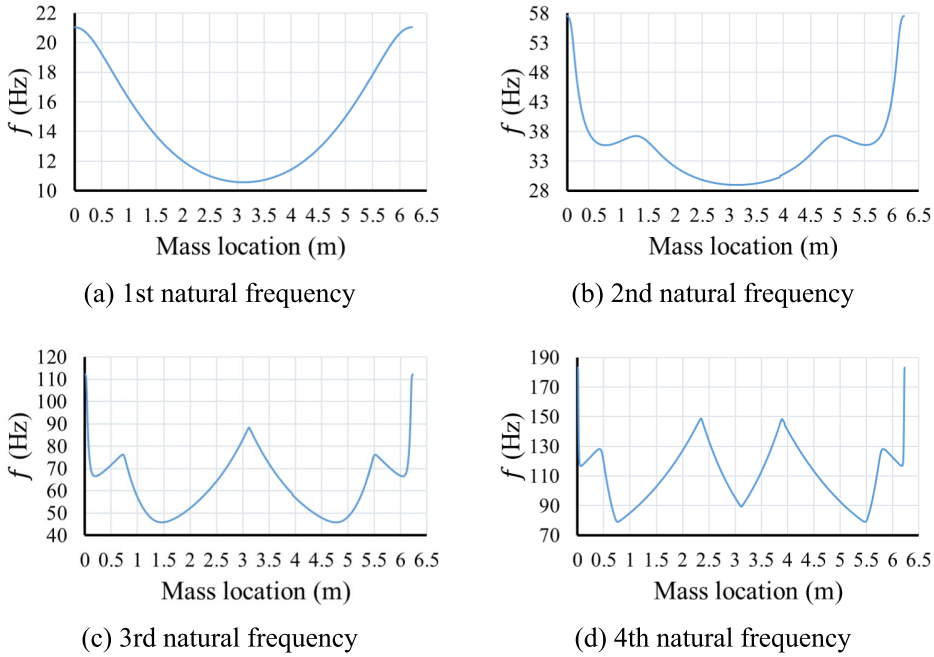

Fig. 19 Natural frequency results of the scaled-up beam (10% crack at 3.94 m)

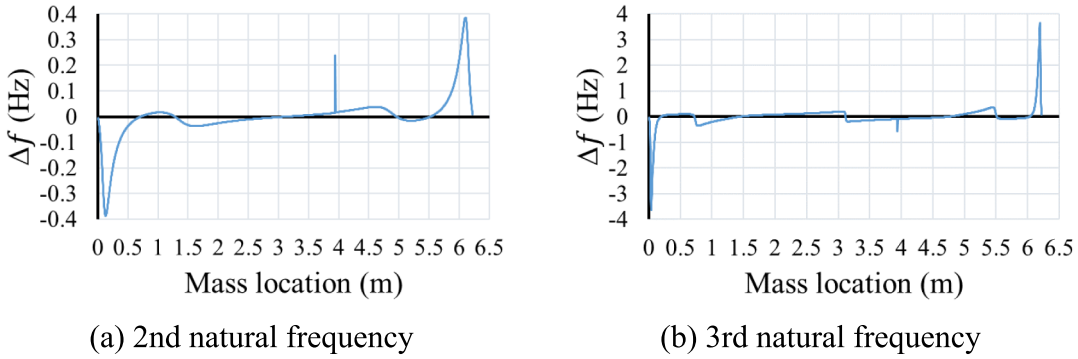

Fig. 20 Natural frequency shift (Δf) results of the scaled-up beam (10% crack at 3.94 m)

The DSM is employed and the Wittrick–Williams algorithm is implemented to search for the natural frequencies.

Figure 19 shows the curves of the first four natural frequencies of the larger beam. For a 10% crack, the frequency change when the mass passing the crack is nearly indistinguishable. When the mass is located close to the boundaries, the effect of the attached mass is reduced and the frequency results approach the natural frequencies of the cracked beam without the mass. As the mass roves away from boundaries, the effect of the mass becomes more significant. Due to this reason, Δf changes rapidly when the mass is near beam boundaries, as shown in Fig. 20.

By focusing only on the results from 0.25 to 6 m, the regions near boundaries are excluded, and the natural frequency shift when the mass passes the crack is highlighted as shown in Fig. 21. Theoretically, the magnitude of Δf when the mass passes the crack should become measurable from the second natural frequency onwards. However, based on the above experimental practice, the value of Δf at the crack location for the second and third natural frequency could be obscured by measurement noise. It might not be until the fourth natural frequency that Δf at the crack location stands out clearly. However, this is still a promising result considering the size of the crack and the relatively low magnitude of the fourth natural frequency.

Figure 22 shows $\Delta(\Delta f)$ as a function of mass location. Unlike Fig. 17 where false peaks are comparable to the peak near the crack location, now the crack can be pinpointed by the notable peak when the mass passes the crack. These results are more promising than the above experimental

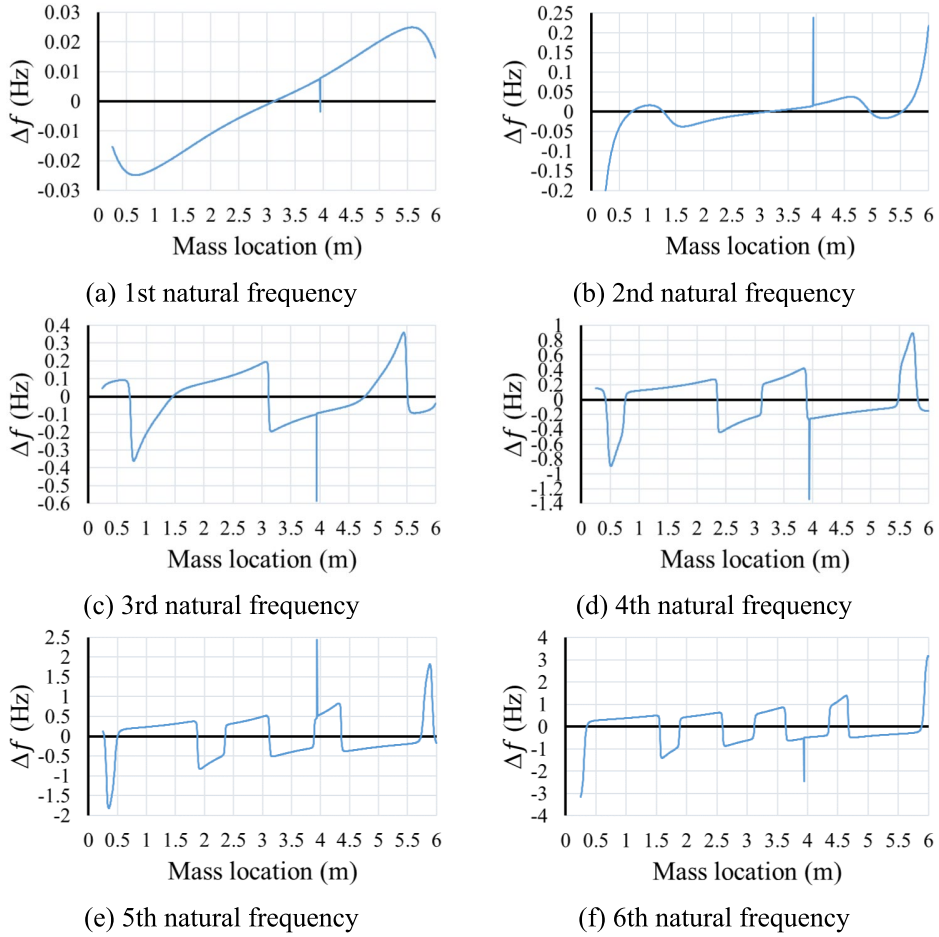

Fig. 21 Natural frequency shift (Δf) results excluding regions near boundaries (10% crack at 3.94 m)

results. However, for the scaled-up beam, 1557 frequency measurements are needed to yield the full frequency curve, which can be a formidable task in practice.

Concluding Remarks

In this study, the theoretical concept of using a roving mass with rotary inertia to locate a crack is verified through experiments. Impact hammer tests were conducted on two cracked beams carrying a roving body with rotary inertia. The natural frequencies obtained through the DSM, FEM, and experimental measurements were in good agreement. It was found that the natural frequency shift when a roving mass with rotary inertia passes a crack can be clearly measured for the 40% cracked beam. For the 20% crack, the natural frequency shift when the mass passes the crack can still be measured, however, it can be difficult to pinpoint the crack location by observing the peak in the curve of Δf or $\Delta(\Delta f)$ versus mass location. Based on the experiments, a larger beam is used in the numerical study and a 10% crack is studied. A step size of about 1/1555 of the beam length proved sufficient for identifying a smaller crack (e.g. a 10% crack) using the first 4 modes. However, reducing the roving step size presents a demanding task to obtain the full frequency curve as a large number of frequency measurements are needed, which can make this method tedious in practice. Overall, this study provides insights into the practical feasibility of the roving mass technique for crack detection. For a medium crack (e.g. a 20–40% crack) in a beam-like structure, it is possible to locate the crack using the measured natural frequency shift. To detect a smaller crack (e.g. a 10% crack), the current method calls for more resources such as noncontact equipment (e.g. scanning laser Doppler vibrometers) and noncontact vision-based vibration measurement [47–49] to facilitate more efficient and accurate frequency measurement.

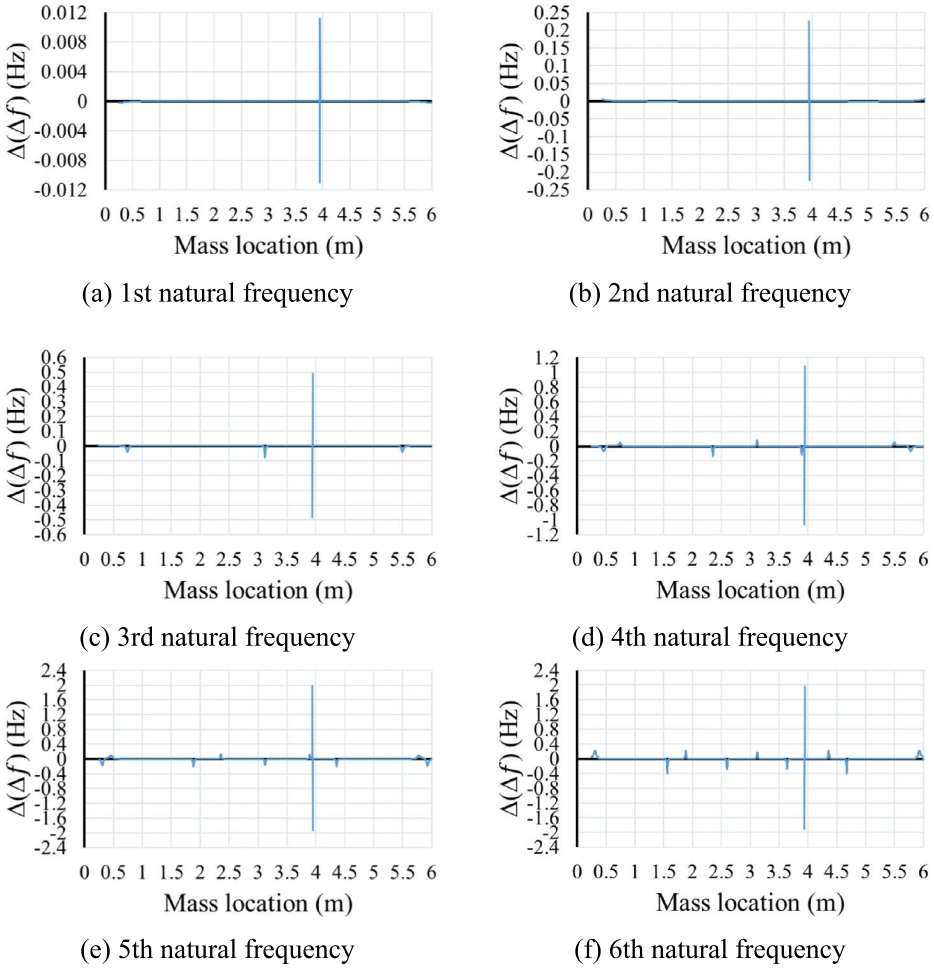

Fig. 22 The change of natural frequency shift excluding regions near boundaries (10% crack at 3.94 m)

Supplementary Information The online version contains supplementary material available at https://doi.org/10.1007/s42417-024-01735-z.

Acknowledgements The first author would like to express deep appreciation to the University of Waikato for the award of a doctoral scholarship, which made this work happen.

Author Contributions X. Sun: methodology, software, validation, formal analysis, investigation, data curation, writing—original draft, visualization. S. Ilanko: conceptualization, methodology, resources, writing—review & editing, supervision, project administration, funding acquisition. Y. Mochida: methodology, writing—review & editing, supervision, resources, project administration, funding acquisition. R.C. Tighe: writing—review & editing, supervision, resources. B.R. Mace: formal analysis, writing—review & editing, resources.

Funding Open Access funding enabled and organized by CAUL and its Member Institutions.

Data availability The data that support the findings of this study are available on request from the corresponding author, Y. Mochida. The data are not publicly available due to privacy restrictions.

Declarations

Conflict of Interests None.

References

1. Gharehbaghi VR, Noroozinejad Farsangi E, Noori M, Yang TY, Li S, Nguyen A, Málaga-Chuquitaype C, Gardoni P, Mirjalili S (2022) A critical review on structural health monitoring: definitions, methods, and perspectives. Arch Comput Methods Eng 29(4):2209–2235. https://doi.org/10.1007/s11831-021-09665-9
2. Doebling SW, Farrar CR, Prime MB (1998) A summary review of vibration-based damage identification methods. Shock Vib Digest 30(2):91–105. https://doi.org/10.1177/058310249803000201

3. Chatzi EN, Papadimitriou C (2016) Identification methods for structural health monitoring. Springer
4. Hadjileontiadis LJ, Douka E, Trochidis A (2005) Crack detection in beams using kurtosis. Comput Struct 83(12):909–919. https://doi.org/10.1016/j.compstruc.2004.11.010
5. Caicedo D, Lara-Valencia L, Valencia Y (2022) Machine learning techniques and population-based metaheuristics for damage detection and localization through frequency and modal-based structural health monitoring: a review. Arch Comput Methods Eng 29(6):3541–3565. https://doi.org/10.1007/s11831-021-09692-6
6. Avci O, Abdeljaber O, Kiranyaz S, Hussein M, Gabbouj M, Inman DJ (2021) A review of vibration-based damage detection in civil structures: from traditional methods to machine learning and deep learning applications. Mech Syst Signal Process. https://doi.org/10.1016/j.ymssp.2020.107077
7. Gomes GF, Mendez YAD, Alexandrino PdSL, da Cunha SS, Ancelotti AC (2019) A review of vibration based inverse methods for damage detection and identification in mechanical structures using optimization algorithms and ann. Arch Comput Methods Eng 26(4):883–897. https://doi.org/10.1007/s11831-018-9273-4
8. Sun X, Ilanko S, Mochida Y, Tighe RC (2023) A review on vibration-based damage detection methods for civil structures. Vibration 6(4):843–875. https://doi.org/10.3390/vibration6040051
9. Al-Said SM (2008) Crack detection in stepped beam carrying slowly moving mass. J Vib Control 14(12):1903–1920. https://doi.org/10.1177/1077546307081321
10. Zhong S, Oyadiji SO (2008) Identification of cracks in beams with auxiliary mass spatial probing by stationary wavelet transform. J Vib Acoust 130(4):041001. https://doi.org/10.1115/1.2891242
11. Yang C, Oyadiji SO (2017) Damage detection using modal frequency curve and squared residual wavelet coefficients-based damage indicator. Mech Syst Signal Process. https://doi.org/10.1016/j.ymssp.2016.06.021
12. Zhang Y, Wang L, Lie ST, Xiang Z (2013) Damage detection in plates structures based on frequency shift surface curvature. J Sound Vib 332(25):6665–6684. https://doi.org/10.1016/j.jsv.2013.07.028
13. Zhang Y, Lie ST, Xiang Z, Lu Q (2014) A frequency shift curve based damage detection method for cylindrical shell structures. J Sound Vib 333(6):1671–1683. https://doi.org/10.1016/j.jsv.2013.11.026
14. Zhong S, Zhong J, Zhang Q, Maia N (2017) Quasi-optical coherence vibration tomography technique for damage detection in beam-like structures based on auxiliary mass induced frequency shift. Mech Syst Signal Process. https://doi.org/10.1016/j.ymssp.2017.02.005
15. Wang L, Lie ST, Zhang Y (2016) Damage detection using frequency shift path. Mech Syst Signal Process. https://doi.org/10.1016/j.ymssp.2015.06.028
16. Lee E-T, Eun H-C (2015) Damage detection using measurement response data of beam structure subject to a moving mass. Lat Am J Solids Struct. https://doi.org/10.1590/1679-78251975
17. Dadoulis GI, Manolis GD (2023) Dynamic response of a damaged bridge model traversed by a heavy point mass. J Sound Vib 551:117613. https://doi.org/10.1016/j.jsv.2023.117613
18. Lie S, Zhang Y, Wang L (2015) Damage detection in compressed natural gas (cng) cylinders based on auxiliary mass induced frequency shift. Exp Mech 55(3):487–498. https://doi.org/10.1007/s11340-014-9960-5
19. Cao L, He W-Y, Ren W-X (2021) Damage localization and quantification for beam bridges based on frequency variation of parked vehicle-bridge systems. Structures 31:357–368. https://doi.org/10.1016/j.istruc.2021.01.098
20. Wang L, Zhang Y, Lie ST (2017) Detection of damaged supports under railway track based on frequency shift. J Sound Vib 392:142–153. https://doi.org/10.1016/j.jsv.2016.11.018
21. Razvarz S, Jafari R, Gegov A (2021) A review on different pipeline defect detection techniques. Flow modelling and control in pipeline systems: a formal systematic approach. Springer International Publishing, Cham, pp 25–57
22. de Morais M, Barbosa E, Silva R, Santos J, Machado M (2020) Damage detection in simple supported pipe conveying fluid using an additional moving mass. In: XLI Ibero-Latin American Congress on Computational Methods in Engineering. Parana, Brazil.
23. Sadeghi MH, Karimi-Dona MH (2011) Dynamic behavior of a fluid conveying pipe subjected to a moving sprung mass—an fem-state space approach. Int J Press Vessels Pip 88(4):123–131. https://doi.org/10.1016/j.ijpvp.2011.02.004
24. Nguyen KV (2016) Crack detection of a double-beam carrying a concentrated mass. Mech Res Commun 75(20):28. https://doi.org/10.1016/j.mechrescom.2016.05.009
25. Haji ZN, Olutunde Oyadiji S (2014) The use of roving discs and orthogonal natural frequencies for crack identification and location in rotors. J Sound Vib 333(23):6237–6257. https://doi.org/10.1016/j.jsv.2014.05.046
26. Cannizzaro F, De Los Rios J, Caddemi S, Caliò I, Ilanko S (2018) On the use of a roving body with rotary inertia to locate cracks in beams. J Sound Vib 425:275–300. https://doi.org/10.1016/j.jsv.2018.03.020
27. Ilanko S, Mochida Y, De Los RJ (2018) Vibration analysis of cracked structures as a roving body passes a crack using the Rayleigh-Ritz method. EPI Int J Eng 1(2):30–34. https://doi.org/10.25042/epi-ije.082018.04
28. Al Jabri AR, Abedin KM, Mujibur Rahman SM (2022) The nyquist criterion and its relevance in phase-stepping digital shearography: a quantitative study. J Mod Opt 69(14):804–810. https://doi.org/10.1080/09500340.2022.2091174
29. Maia NMM, Silva JMM (1997) Theoretical and experimental modal analysis. Research Studies Press
30. e Silva JMM, Maia NMM (1988) Single mode identification techniques for use with small microcomputers. J Sound Vib 124(1):13–26. https://doi.org/10.1016/S0022-460X(88)81403-2
31. Banerjee JR, Ananthapuvirajah A (2019) An exact dynamic stiffness matrix for a beam incorporating rayleigh–love and timoshenko theories. Int J Mech Sci 150:337–347. https://doi.org/10.1016/j.ijmecsci.2018.10.012
32. Banerjee JR, Ananthapuvirajah A (2019) Coupled axial-bending dynamic stiffness matrix for beam elements. Comput Struct 215:1–9. https://doi.org/10.1016/j.compstruc.2019.01.007
33. Papkov SO, Banerjee JR (2015) A new method for free vibration and buckling analysis of rectangular orthotropic plates. J Sound Vib 339:342–358. https://doi.org/10.1016/j.jsv.2014.11.007
34. Banerjee JR, Papkov SO, Liu X, Kennedy D (2015) Dynamic stiffness matrix of a rectangular plate for the general case. J Sound Vib 342:177–199. https://doi.org/10.1016/j.jsv.2014.12.031
35. Tian L, Ye T, Jin G (2021) Vibration analysis of combined conical-cylindrical shells based on the dynamic stiffness method. Thin-Walled Struct 159:107260. https://doi.org/10.1016/j.tws.2020.107260
36. Fazzolari FA (2014) A refined dynamic stiffness element for free vibration analysis of cross-ply laminated composite cylindrical and spherical shallow shells. Compos Part B 62:143–158. https://doi.org/10.1016/j.compositesb.2014.02.021
37. Banerjee JR, Guo S (2009) On the dynamics of cracked beams. In: 50th AIAA/ASME/ASCE/AHS/ASC structures, structural dynamics, and materials conference. California, USA: American Institute of Aeronautics and Astronautics.
38. Su H, Banerjee JR (2013) Free vibration of a cracked timoshenko beam using the dynamic stiffness method. In: 11th international conference on vibration problems. Lisbon, Portugal: Nova University of Lisbon.

39. Caddemi S, Calio I (2013) The exact explicit dynamic stiffness matrix of multi-cracked euler-bernoulli beam and applications to damaged frame structures. J Sound Vib 332(12):3049–3063. https://doi.org/10.1016/j.jsv.2013.01.003
40. Labib A, Kennedy D, Featherston C (2014) Free vibration analysis of beams and frames with multiple cracks for damage detection. J Sound Vib 333(20):4991–5003. https://doi.org/10.1016/j.jsv.2014.05.015
41. Damnjanović E, Marjanović M, Nefovska-Danilović M (2017) Free vibration analysis of stiffened and cracked laminated composite plate assemblies using shear-deformable dynamic stiffness elements. Compos Struct 180:723–740. https://doi.org/10.1016/j.compstruct.2017.08.038
42. Wittrick WH, Williams F (1971) A general algorithm for computing natural frequencies of elastic structures. Quart J Mech Appl Math 24(3):263–284. https://doi.org/10.1093/qjmam/24.3.263
43. Williams F, Wittrick W (1970) An automatic computational procedure for calculating natural frequencies of skeletal structures. Int J Mech Sci 12(9):781–791. https://doi.org/10.1016/0020-7403(70)90053-6
44. Sun X (2021) The application of the wittrick-williams algorithm for free vibration analysis of cracked skeletal structures. Thin-Walled Struct 159:107307. https://doi.org/10.1016/j.tws.2020.107307
45. Zheng DY, Kessissoglou NJ (2004) Free vibration analysis of a cracked beam by finite element method. J Sound Vib 273(3):457–475. https://doi.org/10.1016/S0022-460X(03)00504-2
46. Ewins DJ (2009) Modal testing: theory, practice and application. John Wiley & Sons
47. Javh J, Slavič J, Boltežar M (2017) The subpixel resolution of optical-flow-based modal analysis. Mech Syst Signal Process 88:89–99. https://doi.org/10.1016/j.ymssp.2016.11.009
48. Lin J, Zhong S, Zhang Q, Zhong J, Nsengiyumva W, Peng Z (2022) Swept-source optical coherence vibrometer: principle and applications. IEEE Trans Instrum Meas. https://doi.org/10.1109/TIM.2022.3152238
49. Zhong J, Liu D, Wu S, Li S, Zhong S, Liang W (2022) Three-dimensional translation vibration measurement system based on linear array sensor and composite fringe pattern. Meas Sci Technol 33(9):095901. https://doi.org/10.1088/1361-6501/ac64e8